



# Modeling and Simulation of Fatigue Crack Initiation Process Based on Field Theory of Multiscale Plasticity (FTMP): Part I: PSB Ladder Formation and Verification

You, Xinping

Hasebe, Tadashi

---

**(Citation)**

Metals, 14(12):1392

**(Issue Date)**

2024-12

**(Resource Type)**

journal article

**(Version)**

Version of Record

**(Rights)**

© 2024 by the authors. Licensee MDPI, Basel, Switzerland.

This article is an open access article distributed under the terms and conditions of the Creative Commons Attribution (CC BY) license

**(URL)**

<https://hdl.handle.net/20.500.14094/0100492803>



## Article

# Modeling and Simulation of Fatigue Crack Initiation Process Based on Field Theory of Multiscale Plasticity (FTMP): Part I: PSB Ladder Formation and Verification

Xinping You <sup>1</sup> and Tadashi Hasebe <sup>2,\*</sup> 

<sup>1</sup> Department of Mechanical Engineering, Graduate School, Kobe University, 1-1 Rokkodai-cho, Kobe 657-8501, Japan; you.xinping@mail.mm4.scitec.kobe-u.ac.jp

<sup>2</sup> Department of Mechanical Engineering, Kobe University, 1-1 Rokkodai-cho, Kobe 657-8501, Japan

\* Correspondence: hasebe@mech.kobe-u.ac.jp; Tel.: +81-0788036113

**Abstract:** In this study, we successfully reproduced the persistent slip band (PSB) with ladder patterned morphology, showcasing the predictive capability of the framework of Field Theory of Multiscale Plasticity (FTMP) without relying on ad hoc models, intricate mathematical models, or elaborate finite element discretization. The FTMP-incorporated CP-FEM simulation not only reasonably replicates the experimentally observed ladder morphology and PSB but also effectively simulates surface roughening and grooving, independent of vacancy formation and diffusion. These results highlight the significance of ladder morphology and set the stage for further investigations into the effects of vacancy formation, as extended in the subsequent paper. Leveraging incompatibility tensor-based degrees of freedom, the FTMP framework offers exceptional capabilities for natural modeling dislocation substructures typically overlooked in conventional approaches, positioning it as a transformative tool for advancing our understanding of the mechanisms that dictate slip band-fatigue crack transitions.

**Keywords:** fatigue; persistent slip band; crack initiation; crystal plasticity; field theory; non-Riemannian plasticity; finite element method; vacancy diffusion



**Citation:** You, X.; Hasebe, T.

Modeling and Simulation of Fatigue Crack Initiation Process Based on Field Theory of Multiscale Plasticity (FTMP): Part I: PSB Ladder Formation and Verification. *Metals* **2024**, *14*, 1392. <https://doi.org/10.3390/met14121392>

Academic Editor: Dariusz Rozumek

Received: 30 September 2024

Revised: 23 November 2024

Accepted: 28 November 2024

Published: 4 December 2024



**Copyright:** © 2024 by the authors. Licensee MDPI, Basel, Switzerland. This article is an open access article distributed under the terms and conditions of the Creative Commons Attribution (CC BY) license (<https://creativecommons.org/licenses/by/4.0/>).

## 1. Introduction

Research into metal fatigue has a long-standing history, with significant contributions dating back over half a century. Early investigations by Thompson et al. [1] revealed that fatigue cracks initiate within slip bands of a single grain, highlighting the critical role of microscopic dislocation structures in fatigue crack formation. Building on this foundation, Woods et al. [2] emphasized the presence of persistent slip bands (PSBs), characterized by uniformly arranged dislocation walls, often referred to as ladder walls. Polák et al. [3–6] further explored the relationship between these dislocation substructures and the resultant surface morphology. Essmann et al. [7,8] conducted extensive studies on irreversible deformation associated with the ladder structure of PSBs and its influence on crack initiation at the PSB–matrix interface. They examined the crucial role of vacancies commonly found in fatigued metals [9,10], including their agglomeration into crack nucleation sites.

Subsequent studies have continued to enhance our understanding of the relationship between persistent slip band (PSB) ladder structures and fatigue crack initiation, an inquiry that remains ongoing. Historically, crack initiation modeling continues to be an unsatisfactory endeavor due to its inherent complexities as a whole. A significant portion of the research has focused on interactions with singular interfaces, such as grain and twin boundaries in various practical alloy materials [11–13]. Meanwhile, simulations of crack initiation and subsequent propagation processes have often been limited to scenarios involving artificial notches and stress concentration sites [14], as observed in compact tension

(CT) specimens [15–17], or even from a pre-existing cracks [15,18–20], relying heavily on phenomenological elasto-plasticity and established fracture mechanics.

In recent years, there has been a notable increase in the application of crystal plasticity finite element analysis (CP-FEM) [21–24], which integrates detailed geometric information about microstructures and crystallography. This has been complemented by rapidly advancing experimental observation techniques, including micro-beam X-ray Laue diffraction [25], in situ and ex situ SEM-EBSD (electron backscattering diffraction) [23,26], ECCI (electron channeling contrast imaging) [22], and HR-DIC (high-resolution digital image correlation) [14] analyses. Furthermore, significant progress has been made in coupling simulations with metallurgical microstructure modeling, particularly through the application of discrete dislocation dynamics (DDD) [24,27–29] and phase-field (PF) [30,31] techniques as powerful numerical tools. An extensive review by Sangid [32] highlights the potential of high-precision experimental measurements and computational simulations; however, it does not focus on crack nucleation or the role of dislocation substructures in crack growth and propagation. The interrelationships between dislocation substructures, particularly cell formation, have been suggested in various studies [33–35].

Despite the advances with DDD and PF methods, progress in accurately reproducing the fatigue crack initiation process purely from deformation fields remains limited, without relying on hard spots or similar features. CP-FEM analyses, in particular, are often employed as supporting tools rather than predictive ones, due to inherent limitations in their predictive capabilities, which indicates a lack of standalone competency. This inadequacy in predicting deformation-induced dislocation substructures highlights a significant drawback of conventional CP-FEM, as the slip bands responsible for fatigue crack initiation are closely linked to dislocation substructures that are spontaneously induced during deformation. This limitation is further underscored by the inability to reproduce even simple intragranular banded substructuring with misorientation [21] or to capture fundamental clues to dislocation substructure formation under cyclic straining without resorting to overly complex models [22].

The significance of deformation-induced patterning in plasticity is paramount for understanding the multiscale nature of material mechanics. This importance arises from the dynamic changes in dislocation substructures influenced by long-range stress fields and misorientation, particularly in materials that yield dislocation structures with cellular morphology [36,37]. These dislocation patterns play a crucial role in the storage and release of elastic strain energy, influencing not only the deformation capacity but also the strength and toughness of materials. A notable exception is the ladder structure observed in PSBs, which predominantly facilitates deformation during cyclic loading and typically does not produce a long-range stress field due to its composition of edge dislocation dipoles [38]. This PSB ladder structure significantly impacts the mechanisms of fatigue crack initiation, as previously described [39–43]. However, the underlying reasons for this patterning and its critical roles remain undefined, partly due to limitations in conventional approaches to plasticity.

While analogy-based methods, such as reaction–diffusion equations grounded in the concept of dissipative structures, can address patterning-related issues, they often provide limited insights beyond mere analogy [44,45]. These methods do not elucidate the mechanisms involved in crack initiation. Recent research, fueled by advances in computational capabilities, has increasingly relied on DDDs [27,46,47] and molecular dynamics (MD) simulations [48], employing multiscale methods to model these phenomena. However, these studies often focus narrowly on specific aspects, such as passing stress [38,49], rather than capturing the complete picture that includes the roles of PSB ladders and the processes of crack nucleation, e.g., [48,50].

Modeling fatigue presents significant challenges, particularly concerning crack initiation, as it must consider the effects of dislocation substructures, that is, the laddered morphology in PSBs. The foundational work by Repetto and Ortiz [51] on finite element simulations of fatigue crack initiation emphasized the role of vacancy-induced elongation

in the PSB region, which leads to surface protrusion as a key factor; however, their study did not account for the ladder morphology explicitly. In contrast, Nakai et al. [52–54] reported that cracks primarily evolve from intrusions rather than extrusions. Their research identified a potential critical condition for the transition from intrusions to cracks, based on detailed observations made using atomic force microscopy (AFM) combined with interrupted fatigue tests. According to their findings, extrusions and/or surface reliefs do not develop into cracks. Through their systematic series of studies on several materials, they successfully identified a potential critical condition for the transition from intrusions to cracks, with further details presented in Section 2.

Focusing on the transition from slip bands to cracks, particularly once this critical condition is reached, may provide a more effective framework and minimize ambiguities in the modeling process. Integrating this critical condition with our Field Theory of Multiscale Plasticity (FTMP)-based approach [55–62] can significantly reduce computational costs, as FTMP does not always require intricate fine mesh divisions to reproduce deformation-induced substructural patterns accurately. This versatile theoretical framework facilitates the study of deformation-induced patterning, which is crucial for controlling mechanical properties across multiscale contexts [55,56]. By incorporating a new underlying degree of freedom related to the incompatibility tensor into the hardening law, we enable the autonomous emergence and spontaneous evolution of dislocation patterns that closely resemble experimental observations, as demonstrated in Ref. [57], through straightforward deformation analyses using CP-FEM. This mechanism effectively redistributes excessive elastic strain energy generated during deformation, promoting system-wide equilibrium. In this context, the incompatibility tensor serves as a critical facilitator of energy release, driving the formation of complex dislocation substructures.

This study aims to elucidate the roles of the ladder structure in PSBs on the fatigue crack initiation process through FTMP-incorporated crystal plasticity (CP)-based finite element method (FEM) simulations. Part I of the paper presents a preliminary series of simulations utilizing a simplified vacancy model to examine surface roughening behavior and the subsequent grooving processes.

## 2. Background

Two pivotal research findings have catalyzed the current series of studies. First, Yokoi et al. [63,64] demonstrated that the addition of copper (Cu) to steels can dramatically alter dislocation substructures, transforming them from cellular to planar configurations. This transformation results in finer surface intrusions and extrusions, significantly delaying the initiation of fatigue cracks, as illustrated in Figure 1A. This finding underscores the crucial role of dislocation substructures in influencing the fatigue crack initiation process.

Second, Nakai et al. [52–54] investigated the transition process from slip bands to cracks through a systematically designed series of interrupted AFM observations. They revealed that surface grooving—an evident manifestation of slip bands—evolves into fatigue cracks when the slip distance (or groove depth) exceeds a critical threshold, which varies among different materials, as shown in Figure 1B. This finding highlights a key mechanism that dictates the transition from slip banding to fatigue cracking. Notably, surface reliefs (bottom left) do not contribute to crack formation; only grooves serve as precursors to crack nucleation, at least according to their studies. In this context, the effect of Cu addition on the core structure of screw dislocations in  $\alpha$ -Fe has been studied separately through ab initio calculations [65]. Cross slip by screw dislocations is considered critical for dynamic recovery, which drives cell formation. We reported a transition of the core structure from isotropic to fully extended, a change that tends to inhibit cross slip, thereby hindering dynamic recovery and the resulting cell formation. This provides one possible explanation for why the addition of Cu leads to vein-like or planar dislocation substructures, rather than cellular morphology.

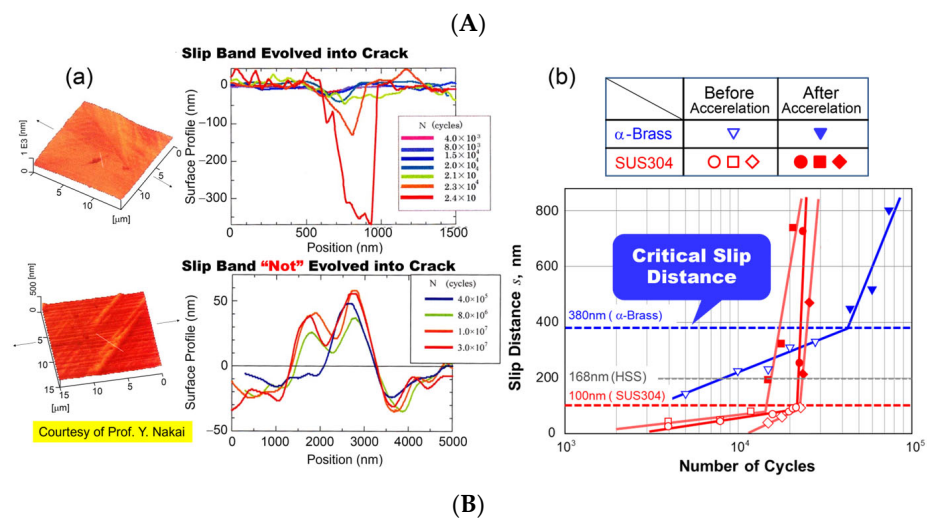
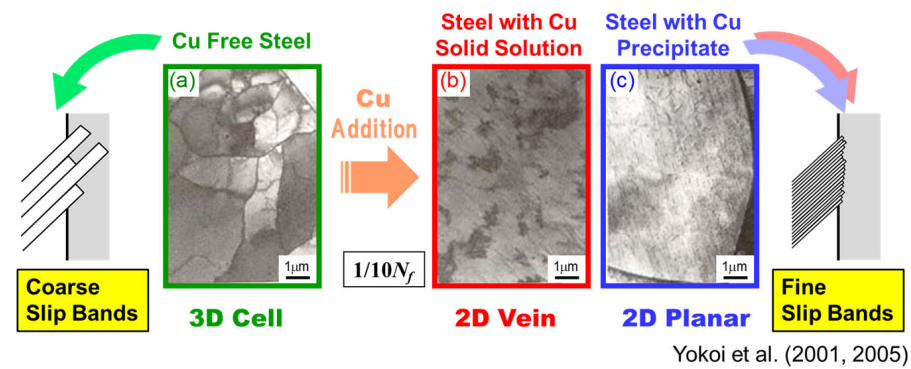


**Figure 1.** Informative experimental results for modeling fatigue crack initiation process. (A) Effect of dislocation substructures on slip banding and fatigue cracking, adapted from Yokoi et al. [63,64] (2001, 2005). (B) Transition of slip bands into cracks, measured by critical slip distance (a) compares surface profile variations with stress cycling and AFM micrographs; (b) shows slip distance variation with cycle number for SUS3004 (red) and α-Brass (blue), with open and solid plots representing data before and after slip distance acceleration, adapted from Nakai et al. [52–54] (Courtesy of Y. Nakai).

By explicitly simulating these critical aspects through deformation analyses, we aim to provide groundbreaking insights that enhance our understanding of the fatigue crack initiation process in practical applications. For the former, the case of copper solid solution yielding a 2D vein structure represents the most fundamental scenario. Here, we confine our focus to the widely observed PSB ladder structure, with other matrix morphologies left for future investigation.

### 3. Theory and Kinematics

#### 3.1. Brief Description About FTMP

The Field Theory of Multiscale Plasticity (FTMP) [55–62] is a comprehensive framework encompassing three critical aspects: (i) evolution, (j) description, and (k) cooperation, as illustrated in Figure 2a. It primarily addresses “inhomogeneously evolving” deformation fields, which typically manifest as dislocation substructures (Figure 2b: simulated examples). Notably, the theory’s ability to describe these aspects of evolution distinguishes it from many others. Furthermore, the interaction formalism facilitates explicit treatments of (k) cooperation across multiple scales (Figure 2f).

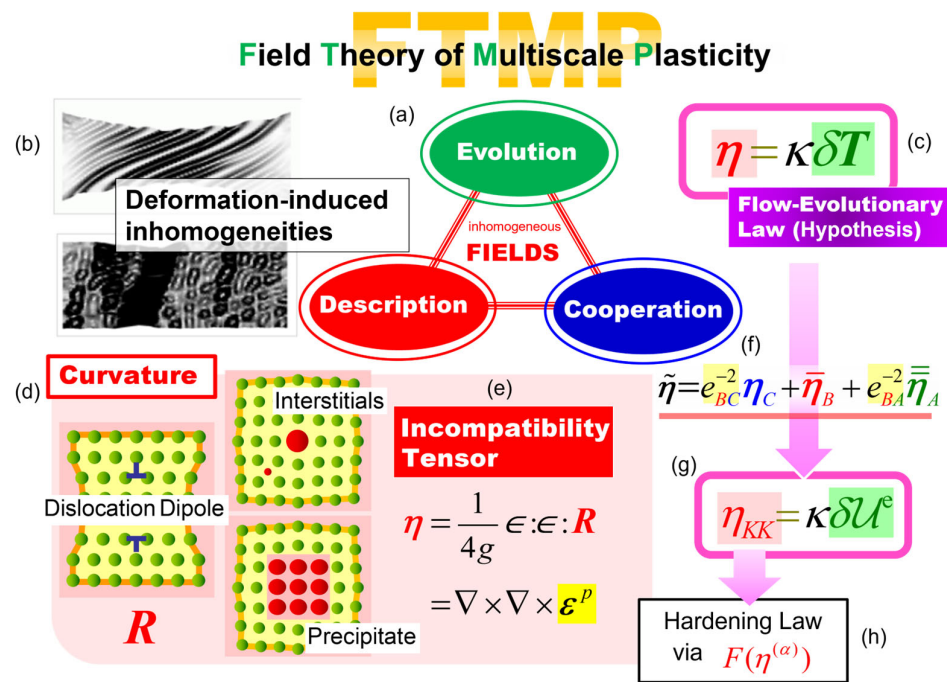


**Figure 2.** Overview of FTMP as a new theory of multiscale plasticity. (a) Key concepts of the FTMP-based framework. (b) Representative simulation results obtained via CP-FEM. (c) The flow-evolutionary law (FEL) as the central concept. (d) Schematic representation of the curvature tensor in differential geometry for describing defect fields in general. (e) Continuum mechanics-based interpretation of the curvature tensor. (f) The interaction formalism represented by the incompatibility tensor field. (g) A specific form of the FEL. (h) The corresponding incompatibility term to be incorporated additively into the hardening law of the CP constitutive equation for CP-FEM simulations.

For the mathematical description of these inhomogeneous fields, differential geometric concepts are predominantly employed, particularly the curvature tensor  $R_{klm}^{::n}$  (Figure 2d) and the torsion tensor  $S_{kl}^{::j}$ , defined respectively as

$$\begin{cases} S_{kl}^{::j} = \Gamma_{[kl]}^j \\ R_{klm}^{::n} = 2 \left[ \partial_{[k} \Gamma_{l]m}^n + \Gamma_{[k|p]}^n \Gamma_{l]m}^p \right] \end{cases} \quad (1)$$

where  $\Gamma_{ij}^k$  represents the coefficient of connection. The significance of utilizing these differential geometric quantities lies in the fact that all imperfections in crystalline space can be completely expressed through them. These tensors correspond to the incompatibility tensor  $\eta_{ij}$  (Figure 2e) and the dislocation density tensor, respectively, drawing on the non-Riemannian plasticity framework advocated by K. Kondo [66,67]. Both can be contracted into second-rank tensors without loss of information by applying the alternating tensor  $\epsilon_{ijk}$  as follows:

$$\begin{cases} \alpha_{ij} = \frac{1}{2} \epsilon_{ikl} S_{kl}^{::j} \\ \eta_{ij} = \frac{1}{4g} \epsilon_{ikl} \epsilon_{jmn} R_{klm}^{::n} (g = \det(g_{ij})) \end{cases} \quad (2)$$

with  $g_{ij}$  being the metric tensor. The incompatibility tensor  $\eta_{ij} = \eta$  is further defined as the double curl of the plastic strain tensor  $\epsilon_{ij}^p = \epsilon^p$  (Figure 2e), while the dislocation density tensor  $\alpha_{ij} = \alpha$  is derived from the curl of the plastic distortion tensor  $\beta_{ij}^p = \beta^p$ .

$$\begin{cases} \alpha_{ij} = - \epsilon_{ikl} \partial_k \beta_{lj}^p \\ \eta_{ij} = \epsilon_{ikl} \epsilon_{jmn} \partial_k \partial_m \epsilon_{ln}^p \end{cases} \text{ or } \begin{cases} \alpha = - \nabla \times \beta^p \\ \eta = \nabla \times \nabla \times \epsilon^p \end{cases} \quad (3)$$

Consequently, strain gradients are intrinsically integrated into the theory. It is important to note that the dislocation density tensor, which represents the first gradient of strain, encompasses the concept of geometrically necessary dislocations (GNDs) [58,60,68]. The component-wise expression of Equation (3) is presented in Appendix A.

At the core of FTMP is the concept known as the “flow-evolutionary law (FEL)”, which serves as a working hypothesis (Figure 2c) [57,59].

$$\eta_{ij} = \kappa \delta T_{ij} \tag{4}$$

where  $\kappa$  refers to the duality coefficient. This relationship connects the incompatibility tensor  $\eta_{ij}$  with the fluctuation of the energy-momentum tensor  $\delta T_{ij} = \delta T$ , where the fluctuation is defined as the deviation from the spatial average, i.e.,  $\delta T_{ij} \equiv T_{ij} - \langle T_{ij} \rangle$ , with  $\langle \cdot \rangle \equiv (1/V) \int (\cdot) dV$ . The incompatibility tensor  $\eta_{ij}$  in this context has been extended to four-dimensional (4D) spacetime (see also Appendix A). The FEL was initially derived in [57] by equating the incompatible displacement with the inhomogeneous force, which are the corresponding conserved quantities of  $\eta_{ij}$  and  $\delta T_{ij}$ , respectively. Details on the energy-momentum tensor and a brief historical background leading to the formulation of the FEL are provided in Appendix B.

The FTMP framework extensively utilizes the incompatibility tensor,  $\eta_{ij}$ , among other elements. Its enhanced applications, presented in Figure 3, are categorized into three aspects: an extended definition to four-dimensional (4D) spacetime, the flow-evolutionary hypothesis (Equation (4)), and the interaction formalism applicable across multiple scales. The 4D-extended definition of  $\eta_{ij}$  is expressed as

$$\eta_{ij} = \epsilon_{iklp} \epsilon_{jmnp} \partial_k \partial_m \epsilon_{ln}^p \tag{5}$$

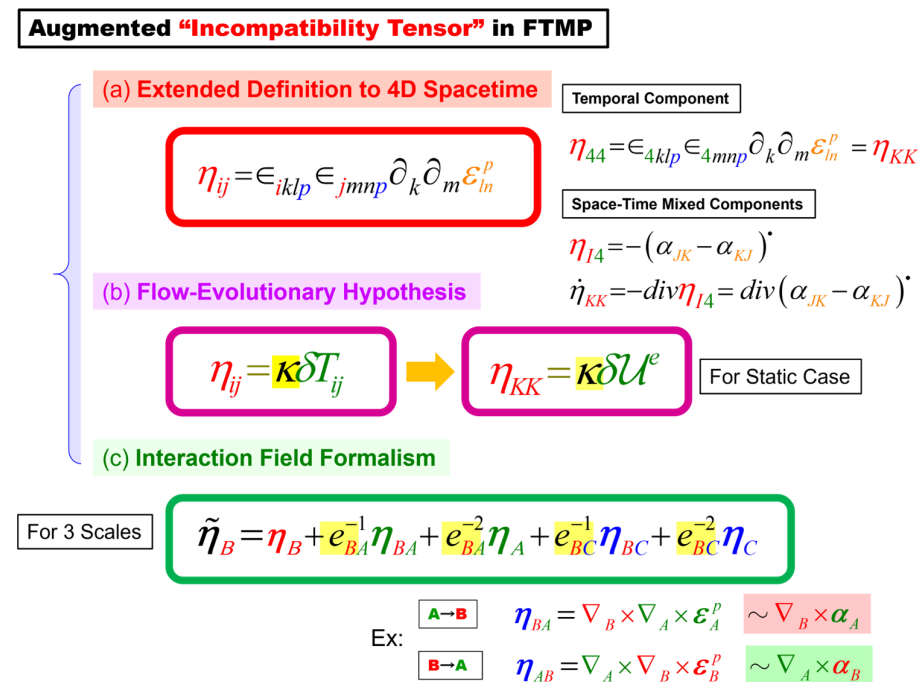


**Figure 3.** Augmented “incompatibility tensor” in FTMP: (a) extended definition of the incompatibility tensor into 4D spacetime, with two specific components of pure temporal and space-time mixed, (b) flow-evolutionary law as working hypothesis, with the specific form for duality diagram presentation scheme (pointed by right arrow), and (c) interaction formalism, presented for three scale problem with Scales A, B and C, with explicit examples for Scale A to B or Scale B to A interactions.

In this context, the indices indicated by lowercase letters denote four-dimensional spacetime (1, 2, 3 for spatial dimensions and 4 for time), while capital letters are used

for spatial components when necessary for clarity. The pure temporal component of the 4D-extended incompatibility tensor  $\eta_{44}$  results in the spatial trace, represented as

$$\eta_{44} = \epsilon_{4klp} \epsilon_{4mnp} \partial_k \partial_m \epsilon_{ln}^p = \eta_{KK} = \text{tr}^{sp} \boldsymbol{\eta} \quad (6)$$

A detailed process for achieving the above relationship is provided in Appendix A. Thus, the pure temporal component of Equation (4) becomes

$$\eta_{KK} = \kappa \delta(U^e + \mathcal{K}) \quad (7)$$

where  $U^e$  denotes the elastic strain energy, and  $\mathcal{K}$  represents the kinetic energy. In static conditions, as is often the case, this simplifies to

$$\eta_{KK} = \kappa \delta U^e \quad (8)$$

as presented in Figure 2g. Equation (8) visualizes the dynamic interrelationships between excessive strain energy being converted or redistributed into the incompatibility-related degrees of freedom, which drive the field evolutions during the course of elasto-plastic deformation.

In practice, there is no need to directly solve Equation (8). Instead, we can incorporate the incompatibility-based underlying degrees of freedom into the hardening law of the constitutive equation used in CP-FEM simulations, as detailed separately below (also see Figure 2h). This integration allows the system to autonomously manage excessive storage of elastic strain energy, leading to significant field evolutions, such as substructure formation. In this context, the evolution of dislocation substructures arises naturally from system-wide accommodations facilitated by incompatibility. If this approach is correct, the necessary dislocation patterning can spontaneously emerge, provided that we properly integrate the incompatibility-related degrees of freedom into the simulation; otherwise, it may not occur. Thus, we anticipate that the ladder-like patterning in PSBs can be effectively reproduced without the need for any ad hoc models, underscoring the robustness of the FTMP framework.

The divergence-free condition for the incompatibility tensor in the 4D spacetime reads

$$\text{div}^{4D} \boldsymbol{\eta} = 0 \Leftrightarrow \dot{\eta}_{44} + \text{div} \eta_{A4} = 0 \quad (9)$$

Here,  $\dot{\eta}_{44} = \dot{\eta}_{KK}$  according to Equation (3), while the space-temporal mixed component  $\eta_{4A}$  is given as

$$\eta_{A4} = -(\alpha_{BC} - \alpha_{CB})^\bullet \quad (10)$$

Ultimately, we establish the following relationship between the incompatibility rate and the edge dislocation density flux by substituting Equation (10) into Equation (9).

$$\dot{\eta}_{KK} = \text{div}(\alpha_{BC} - \alpha_{CB})^\bullet \quad (11)$$

This relationship allows multiple interpretations regarding pair-wise dislocation creation and annihilation processes, making it useful for modeling various detailed processes related to dislocation fields. For a detailed derivation of Equation (11) from Equation (9), refer to Appendix C. The present study utilizes this model to investigate vacancy sources arising from the pair annihilation of edge dislocations in Part II [69].

### 3.2. Kinematics of Crystal Plasticity

The FTMP concepts can be integrated with the conventional kinematics framework of crystal plasticity [70,71], serving as a foundational vehicle for their application. We essentially adhere to this framework, beginning with Lee's elastic-plastic decomposition of the deformation gradient tensor to accurately capture the finite deformation conditions.

$$\mathbf{F} = \mathbf{F}^* \cdot \mathbf{F}^p \quad (12)$$

where  $F^*$  accounts for elastic deformation, including lattice rotation, and  $F^p$  serves as its plastic counterpart.

The constitutive equation for elasticity in a rate form, suitable for finite crystal plasticity, is expressed as

$$(\tau_{(J)}^*)^\circ = C^e : d^* \text{ with } (\tau_{(J)}^*)^\circ = \sigma^\circ + \sigma \cdot \text{tr} d \tag{13}$$

where  $(\tau_{(J)}^*)^\circ$  is the Jaumann rate of the Kirchhoff Stress tensor, viewed from an observer on the rotating lattice.  $\sigma$  expresses the Cauchy stress tensor,  $C^e$  is the elasticity tensor, and  $d^*$  represents the elastic part of the strain rate tensor  $d$ . The relation  $\dot{J} = \text{tr} d = \text{tr} d^*$  has been used in the second equation, with  $\dot{J}$  denoting the Jacobian rate.

Ultimately, we reach

$$\tau_{(J)}^\circ = C^e : d - \sum_{\alpha=1}^N R^{(\alpha)} \dot{\gamma}^{(\alpha)} \text{ with } \begin{cases} R^{(\alpha)} = C^e : P^{(\alpha)} + \beta^{(\alpha)} \\ \beta^{(\alpha)} = W^{(\alpha)} \cdot \sigma - \sigma \cdot W^{(\alpha)} \end{cases} \tag{14}$$

Here,  $P^{(\alpha)} = (\mathbf{s}^{(\alpha)} \otimes \mathbf{m}^{(\alpha)})_{sym}$  and  $W^{(\alpha)} = (\mathbf{s}^{(\alpha)} \otimes \mathbf{m}^{(\alpha)})_{skew}$  are evaluated using the unit vectors for the slip direction  $\mathbf{s}^{(\alpha)}$  and slip plane normal  $\mathbf{m}^{(\alpha)}$ , with  $(\alpha)$  referring to the slip systems. The plastic distortion tensor  $\beta^p$  and plastic strain tensor  $\epsilon^p$  are evaluated, respectively, as

$$\begin{cases} \beta^p = \sum_{\alpha=1}^N (\mathbf{s}^{(\alpha)} \otimes \mathbf{m}^{(\alpha)}) \gamma^{(\alpha)} \\ \epsilon^p = \sum_{\alpha=1}^N P^{(\alpha)} \gamma^{(\alpha)} (= (\beta^p)_{sym}) \end{cases} \text{ with } \gamma^{(\alpha)} = \int \dot{\gamma}^{(\alpha)} dt \tag{15}$$

which are used to explicitly compute the dislocation density and the incompatibility tensors, as defined in Equation (3).

### 3.3. Constitutive Equation for CP-FEM

We employ the general constitutive equation proposed in [57,62] based on dislocation dynamics, applicable both to FCC and BCC metals in a wide range of strain rate and temperature including impact loading conditions. The explicit form is given by

$$\begin{cases} \dot{\gamma}^{(\alpha)} = \dot{A}_{SR} \tau^{*(\alpha)} \left[ \left| \tau^{*(\alpha)} \right| B_{SR} \exp \left( 1 - \left| \frac{\langle \tau^{(\alpha)} - \tau_{Peierls}^{*(\alpha)} \rangle - \Omega^{(\alpha)}}{K^{(\alpha)}} \right|^p \right)^q + C_{SR} \right] \\ \tau^{*(\alpha)} \equiv \langle \tau^{(\alpha)} - \tau_{Peierls}^{*(\alpha)} \rangle - \Omega^{(\alpha)} \end{cases} \tag{16}$$

with  $\dot{A}_{SR} = \rho_m b L v^*$ ,  $B_{SR} = \Delta G_0^{disloc} / kT$ ,  $C_{SR} = B L v^* / b$ , where  $K^{(\alpha)}$  and  $\Omega^{(\alpha)}$  are drag stress and back stress, respectively, responsible for isotropic and kinematic types of hardening. Here,  $\rho_m$ ,  $L$ ,  $v^*$ ,  $b$  and  $B$  are mobile dislocation density, mean flying distance of dislocations, the modified Debye frequency, the magnitude of Burgers vector, and the damping coefficient due to, e.g., phonon drag, respectively, and  $\Delta G_0^{disloc} \equiv \mu(T) b^3 g_0^{disloc}$  stands for the activation energy for dislocation processes at  $T = 0$  K, with  $g_0^{disloc}$  being the normalized one and  $\mu(T)$  the temperature-dependent shear modulus. For BCC metals, we can set  $C_{SR} = 0$ , whereas for FCC we may normally assume  $\tau_{Peierls}^{*(\alpha)} = 0$ . The exponents  $p$  and  $q$  are the parameters specifying the thermal obstacle of interest, provided  $0 \leq p \leq 1$  and  $1 \leq q \leq 2$ . In the above case, a pair of values,  $p = 1/2, q = 3/2$ , is used for representing dislocation processes. Furthermore,  $\langle \circ \rangle \equiv (\circ + |\circ|) / 2$  represents the Mackauley

parenthesis, with  $\tau_{Peierls}^{*(\alpha)}$  expressing the effective stress for the Peierls overcoming process given by

$$\tau_{Peierls}^{*(\alpha)} = \hat{\tau}_{Peierls}^* \left[ 1 - \left( B_{SR}^{p-1} \ln \frac{\dot{\gamma}_{0P}}{\dot{\gamma}^{(\alpha)}} \right)^{1/q_P} \right]^{1/p_P} \quad (17)$$

where  $B_{SR}^{p-1} = kT/g_0^{Peierls} \mu b^3$  with  $g_0^{Peierls}$ ,  $\dot{\gamma}_{0P}$ ,  $p_P$ , and  $q_P$  are parameters for the thermal activation processes via the Peierls overcoming mechanism. The present study neglects the back stress, i.e.,  $\Omega^{(\alpha)} = 0$ , for simplicity. The evolution of the drag stress  $K^{(\alpha)}$  is governed by

$$\begin{cases} \dot{K}^{(\alpha)} = Q_{\alpha\beta} H(\gamma) |\dot{\gamma}^{(\beta)}| \\ Q_{\alpha\beta} = \delta_{\alpha\beta} + f_{\alpha\kappa} S_{\kappa\beta} + F_k(\alpha_k^{(\beta)}; \eta_k^{(\beta)}) \end{cases} \quad (18)$$

where  $Q_{\alpha\beta}$  is the hardening ratio that accounts for additional hardening or softening from the straining/loading history,  $H(\gamma)$  represents the referential hardening moduli,  $H(\gamma) = h_0 \{ (h_0/n\tau_0)\gamma + 1 \}^{n-1}$  with  $\gamma = \sum_{\alpha} \gamma^{(\alpha)}$ ,  $f_{\alpha\beta}$  is the interaction matrix for pairwise dislocation reactions, and  $S_{\kappa\beta}$  expresses a history matrix, further given as an increasing function of plastic work performed by the effective stress that is responsible for dislocation processes, e.g.,  $S_{\alpha\beta} = \tanh(W_{\alpha\beta}^{p*}/W_{sat}^p)$  with  $W_{p*}^{(\beta)} = \int \langle \tau^{(\alpha)} - \tau_{Peierls}^{*(\alpha)} \rangle \cdot \dot{\gamma}^{(\alpha)} dt$  and  $W_{sat}^p$  the saturation value. The FTMP-based strain gradient term  $F_k(\alpha_k^{(\alpha)}; \eta_k^{(\alpha)})$  collectively represents the strain gradient terms for the dislocation density and incompatibility fields; the explicit forms are given as [57–59,62].

$$\begin{cases} F(\alpha^{(\alpha)}) = k_{p_\alpha} \left( \frac{|\alpha^{(\alpha)}|}{b} \right)^{1/2} \\ F(\eta^{(\alpha)}) = \text{sgn}(\eta^{(\alpha)}) \cdot k_{p_\eta} \left( \frac{l_{defect}}{b} |\eta^{(\alpha)}| \right)^{1/2} \end{cases} \quad (19)$$

The parameters include  $l_{defect}$  that represents the targeted inhomogeneous fields, which coincides with the Burgers vector  $b$  in the case of individual dislocations, along with the coefficients  $k_{p_\alpha}$  and  $k_{p_\eta}$ . For evaluating the slip system-wise dislocation density and incompatibility fields, the following projections are employed [57,62]:

$$\begin{cases} \alpha^{(\alpha)} = (\mathbf{t}^{(\alpha)} \otimes \mathbf{s}^{(\alpha)} + \mathbf{s}^{(\alpha)} \otimes \mathbf{s}^{(\alpha)}) : \boldsymbol{\alpha} \\ \eta^{(\alpha)} = (\mathbf{t}^{(\alpha)} \otimes \mathbf{s}^{(\alpha)} + \mathbf{s}^{(\alpha)} \otimes \mathbf{s}^{(\alpha)} + \mathbf{s}^{(\alpha)} \otimes \mathbf{m}^{(\alpha)}) : \boldsymbol{\eta} \end{cases} \quad (20)$$

where  $\mathbf{t}^{(\alpha)} = \mathbf{s}^{(\alpha)} \times \mathbf{m}^{(\alpha)}$  represents the line direction in the case of dislocations. Note that the choice of projection directions can affect the evolved patterning, requiring careful attention, especially regarding the incompatibility term, whereas the dislocation density tensor has a clear physical meaning, specifically representing the edge and screw components via  $\mathbf{t}^{(\alpha)} \otimes \mathbf{s}^{(\alpha)}$  and  $\mathbf{s}^{(\alpha)} \otimes \mathbf{s}^{(\alpha)}$  projections, respectively.

#### 4. Model and Analytical Condition

The finite element (FE) model used for the preliminary analyses is illustrated in Figure 4, which also outlines the analytical conditions. This model, oriented along a single slip direction [152], is discretized into  $24 \times 80 \times 4$  crossed-triangular elements. The evaluation radius for the strain gradient calculation is set to  $r_{GR} = 1.0 \mu\text{m}$ , within which the average slope of the strain values is determined using the least squares method. Cyclic straining is applied under conditions controlled by the plastic strain amplitude of  $\Delta\varepsilon^p/2 = 0.6\%$ .

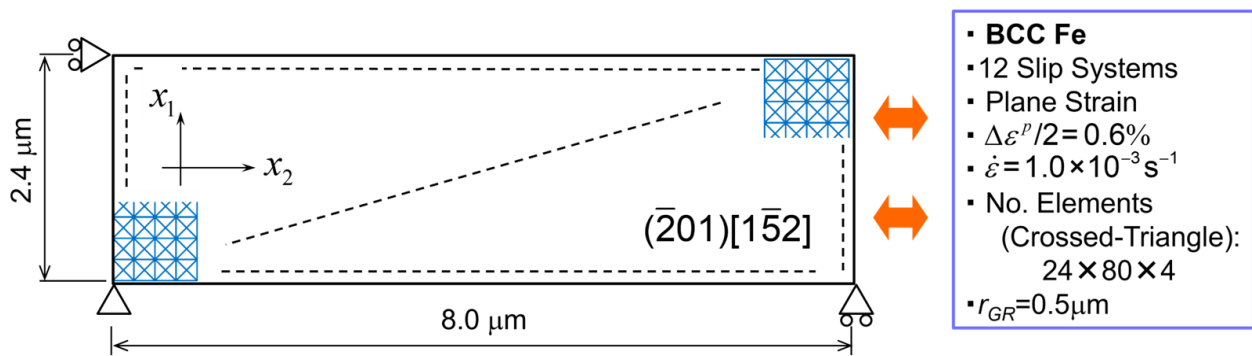


**Figure 4.** FE model for preliminary analyses: single slip-oriented single crystal. Triangles on the model boundary represent constraint conditions, where displacements are fixed in all directions, except in the rolling direction, which is specified by the pair of rollers at the bottom.

The present study focuses on commercially pure iron (Fe), with the aim of expanding the discussions about Cu-added steels described in conjunction with Figure 1A. In future research, we plan to explore the influence of dislocation substructures on slip band formation and the subsequent transition to crack propagation. All material parameters utilized in the current series of simulations, including those for  $F_k(\alpha_k^{(\alpha)}; \eta_k^{(\alpha)})$  in Equation (18), are listed in Table 1, while those for  $f_{\alpha\beta}$  in Equation (17) are summarized in Table 2 [57].

**Table 1.** Material parameters used in CP-FEM simulations, adapted from [57].

Category	Parameter	Value
Shear Strain Rate $\dot{\gamma}^{(\alpha)}$	$\dot{A}_{SR}[/s]$	$2.75 \times 10^{10}$
	$B_{SR}$	145.5
	$p$	0.67
	$q$	2.0
Peierls Stress $\tau_{Peierls}^{(\alpha)}$	$\dot{\gamma}_{0P}[/s]$	$8.75 \times 10^6$
	$\hat{\tau}_{Peierls}^*$ [MPa]	356
	$B_{SR}^p$	3.493
	$p_P$	0.83
	$q_P$	2.0
	$\mu$	(= $C_{44}$ )
Drag Stress $K^{(\alpha)}$	$h_0$	$1.0 \times 10^4$
	$\tau_0$ [MPa]	116
	$W_{sat}^P$	6.0
	$n$	0.13
Shear Gradient Terms $F(\alpha^{(\alpha)}; \eta^{(\alpha)})$	$k_{p_\alpha}$	0.2
	$k_{p_\eta}$	0.1
	$l_{defect}$ [ $\mu\text{m}$ ]	10.0
	$b$ [m]	$2.48 \times 10^{-10}$
Elastic Stiffness $C_{ij}$ [GPa]	$C_{11}$	237
	$C_{12}$	141
	$C_{44}$	116

**Table 2.** Interaction matrix for dislocation pairs for BCC metals. adapted from [57].

	1	2	3	4	5	6	7	8	9	10	11	12
1	1.065											
2	0	1.065										
3	0	0	1.065									
4	0	0	0	1.065								
5	1.48	1.343	1.343	0	1.065							
6	1.343	1.48	0	1.343	0	1.065						
7	1.343	0	1.48	1.343	0	0	1.065					
8	0	1.343	1.343	1.48	0	0	0	1.065				
9	1.48	1.343	0	1.343	1.48	0	1.343	1.343	1.065			
10	1.343	1.48	1.343	0	0	1.48	1.343	1.343	0	1.065		
11	0	1.343	1.48	1.343	1.343	1.343	1.48	0	0	0	1.065	
12	1.343	0	1.343	1.48	1.343	1.343	0	1.48	0	0	0	1.065
System Number	1	2	3	4	5	6	7	8	9	10	11	12
Schmid and Boas	B5	C5	D6	A6	B4	C3	D4	A3	B2	C1	D1	A2
Burgers vectors	111	11 $\bar{1}$	1 $\bar{1}$ 1	1 $\bar{1}\bar{1}$	111	11 $\bar{1}$	1 $\bar{1}$ 1	1 $\bar{1}\bar{1}$	111	11 $\bar{1}$	1 $\bar{1}$ 1	1 $\bar{1}\bar{1}$
Slip planes	1 $\bar{1}$ 0	1 $\bar{1}$ 0	110	110	10 $\bar{1}$	101	10 $\bar{1}$	101	01 $\bar{1}$	011	011	01 $\bar{1}$

## 5. Results and Discussion

### 5.1. General Features

Figure 5 presents a simulated incompatibility contour on a representative slip system ( $\alpha$ ) along with its projected counterpart on the primary slip system ( $\beta$ ), based on the process

$$\langle F(\eta^{(\alpha)}) \rangle_{\text{projected}} \equiv \sum_{\beta=1}^n (\mathbf{m}_{\text{primary}}^{(\alpha)} \cdot \mathbf{m}^{(\beta)}) F(\eta^{(\beta)}) \quad (21)$$

where  $\mathbf{m}^{(\alpha)}$  represents the slip plane normal, and the subscript “primary” specifies that for the primary system as  $\mathbf{m}_{\text{primary}}^{(\alpha)}$ . As confirmed in Figure 5b, the projection onto the primary slip plane effectively cancels the incompatibility pattern in the matrix region, leaving only the ladder-like pattern along the slip band. This suggests that the incompatibility-based patterning can essentially be categorized as a fluctuation, resulting in a net value of zero overall, in general. In contrast, the dislocation density contour, represented by the edge component  $\alpha_{31}$  shown in Figure 5c, naturally exhibits a ladder-like structure, even without this projection. This indicates that the resultant dislocation substructure corresponds to the projected incompatibility distribution.

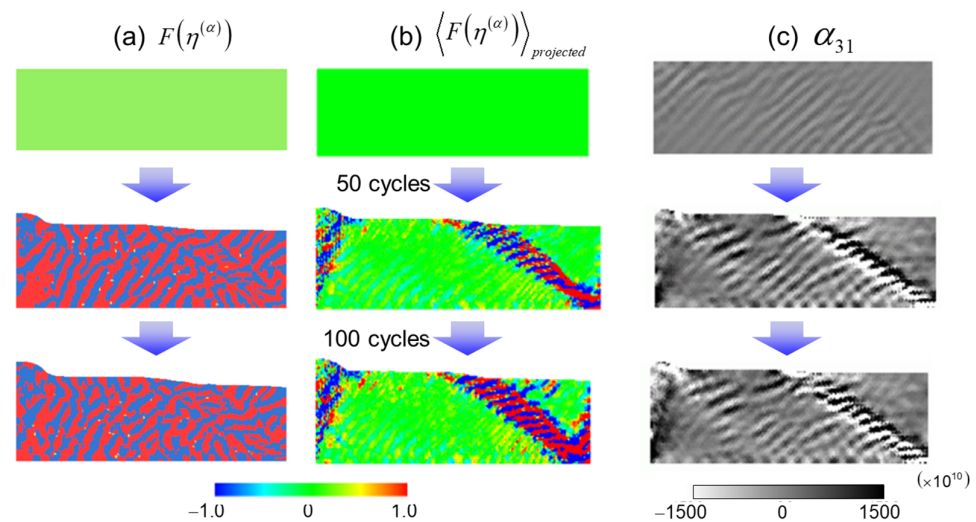


**Figure 5.** Incompatibility contours before and after projection onto the primary slip plane (via Equation (20)), together with dislocation density contour.

The reproduced PSB accompanied by ladder-like patterning, as anticipated above (see Section 3.1), underscores the predictive power of the FTMP framework, without any additional ingredients nor specifically-designated intricate mathematical models; moreover, essentially there is no need for elaborate finite element discretization. This reinforces our confidence in modeling seamlessly the fatigue crack initiation processes that such specific dislocation structures can be accurately reproduced without reliance on ad hoc models.

To demonstrate how the ladder-patterned region is softened, the sample is monotonically pulled after interrupting the cyclic straining. Figure 6a compares the samples pulled before the onset of cyclic straining (0 cycles) and after 80 cycles. As expected, the ladder-patterned sample exhibits landslide-like localized deformation, while the 0-cycle sample shows relatively uniform elongation. The results of monotonic tension after various straining cycles are presented in Figure 6b, indicating that 15 cycles of straining lead to complete softening of the PSB.

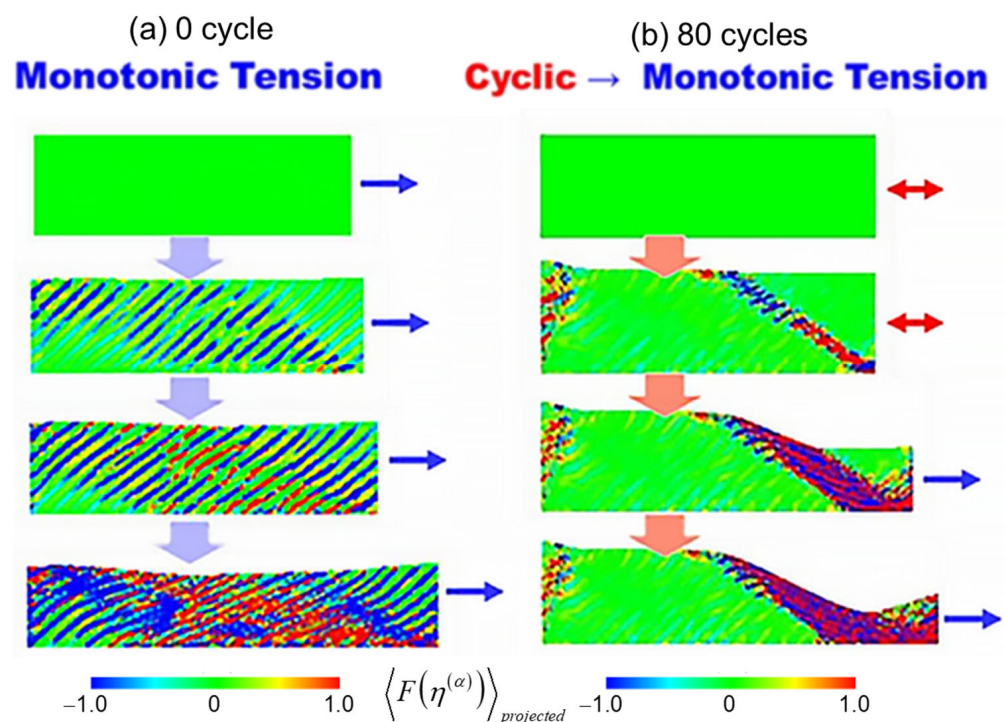


**Figure 6.** Comparison of sample deformation under monotonic tension (a) before (i.e., 0 cycle) and (b) after 80 cycles of cyclic straining (see Figure 7i), illustrating that the ladder-like region has been significantly softened.

Figure 8 compares the hysteresis loops for the matrix and PSB regions. The PSB region exhibits a plastic strain amplitude three times larger, highlighting strain localization along the ladder-like band, with this region accounting for approximately 14% of the total volume. Notably, the loop for the PSB region tends to shift toward the tension side to balance system-wide deformation, ensuring symmetric push–pull straining. It is worth mentioning that this concentration of deformation is less than what is typically observed in reality, primarily because the present simulation does not distinctly capture vein structures in the matrix region, which can impede deformation. However, reproducing the vein morphology in the matrix is not within the scope of this study at this stage.

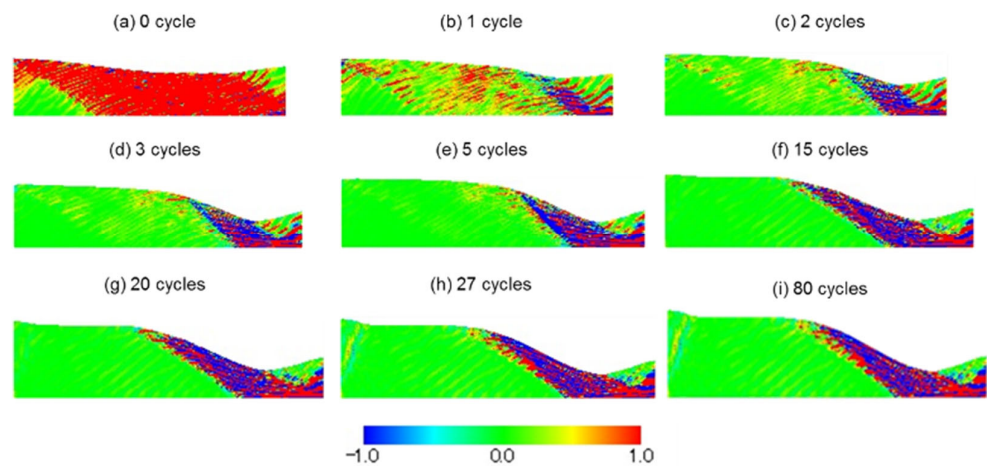


**Figure 7.** Comparison of sample deformation under monotonic tension for samples interrupted after various cyclic strain cycles. The labels (a) through (i) indicate the specific interrupting cycles: (a) 0, (b) 1, (c) 2, (d) 3, (e) 5, (f) 15, (g) 20, (h) 27, and (i) 80 cycles, respectively.

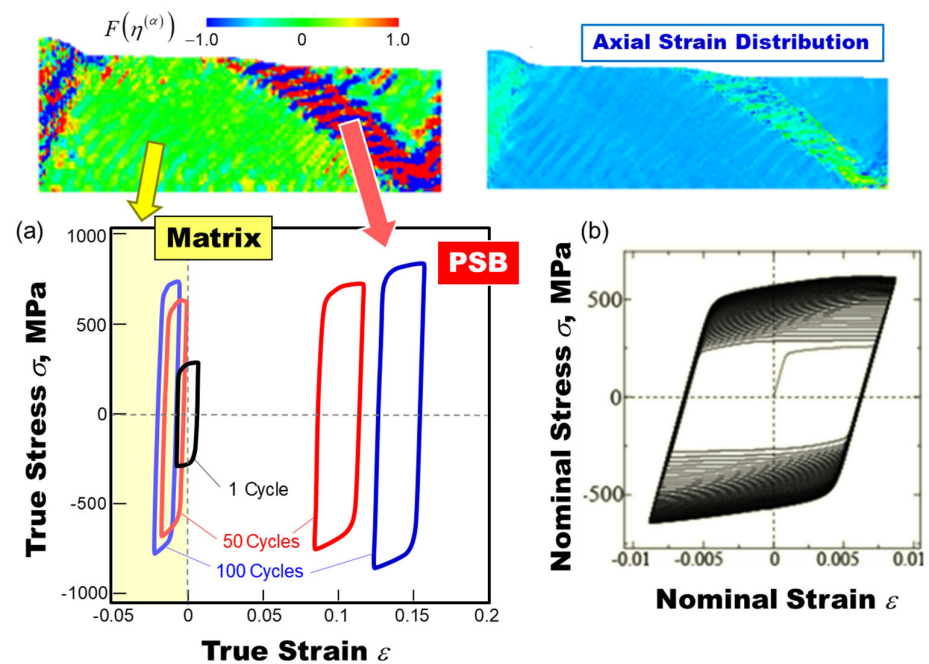


**Figure 8.** Comparison of simulated hysteresis loops between the matrix and PSB regions, (a) the matrix and (b) PSB regions.

### 5.2. Specific Features

Let us examine how the reproduced patterns reflect reality. Figure 9 analyzes the ladder region in terms of component-wise dislocation density distribution, while Figure 10 illustrates the growth of their cross-sectional distributions with increasing straining cycles. Here, we display  $\alpha_{22}$  and  $\alpha_{31}$  as representatives for the screw and edge components, respectively, while  $\alpha_{11}$  and  $\alpha_{32}$  show similar trends, although it is not presented. The following points are clearly demonstrated: first, the ladder morphology comprises both screw and edge dislocation components; second, these components are alternately aligned, closely resembling experimental observations, as also confirmed in Figure 10. Furthermore, there is essentially no misorientation developed throughout the sample, with a deviation of less than 1 degree, consistent with experimental observations. To be noted is that

incompatibility-induced substructures are accompanied by misorientation developments in general.

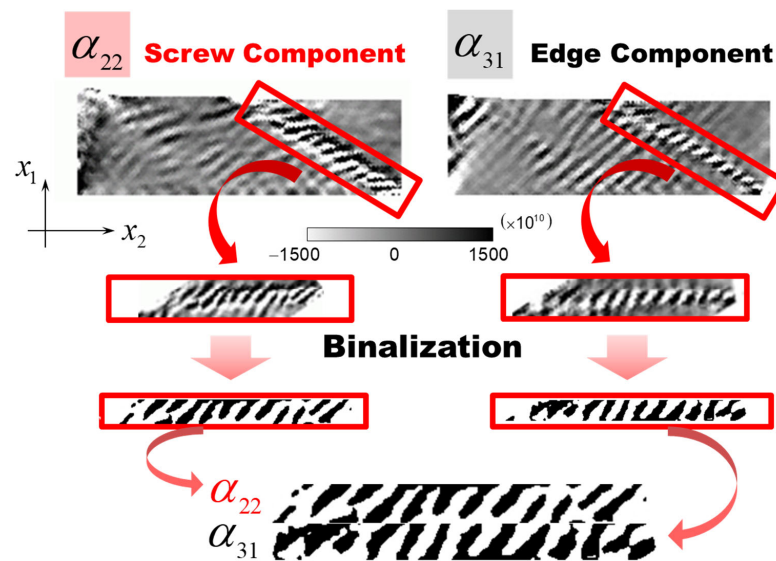


**Figure 9.** Comparison of dislocation density contours between edge and screw components, where binalized versions are rearranged vertically in the bottom for making comparison easier.

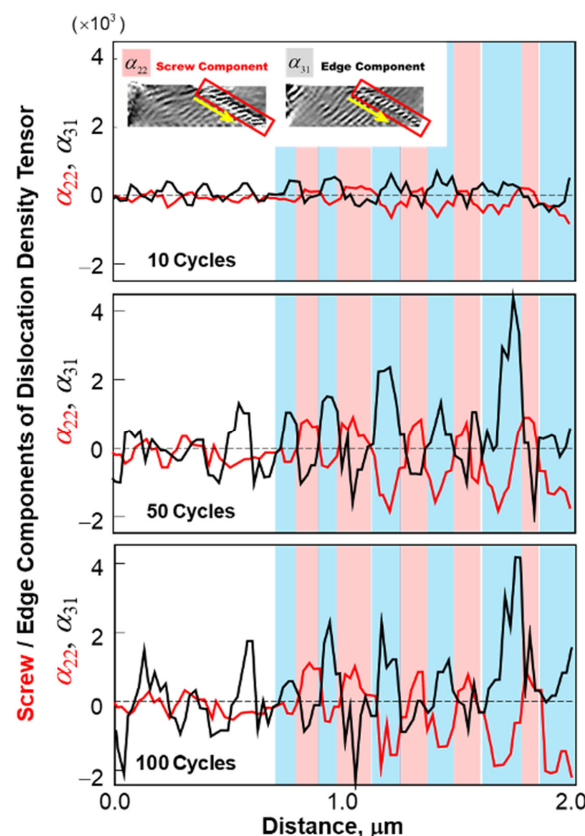


**Figure 10.** Cross-sectional distributions of dislocation density along PSBs ( $x$ -axis) comparing two components of dislocation density tensor, i.e., screw and edge, at 10, 50, and 100 cycles. Background coloring highlights areas with positive values for both components, making them easier to visualize. The red boxes in the inset show the PSB section where the distribution is measured, and the yellow arrows indicate the measurement direction, starting from the surface, corresponding to the horizontal axis.

On the less desirable side, we observe a slightly larger amplitude for  $\alpha_{31}$  than for  $\alpha_{22}$  in Figure 10, indicating that the structure is less capable of carrying deformation, as the screw segments play a key role in this capacity. This also contributes to the previously mentioned smaller strain concentration, alongside the less-developed vein-like morphology in the matrix region. Additionally, another difference remains in the width ratio of the ladder wall to channel regions, which ought to be much smaller, indicating potential room for further improvement.

### 5.3. Surface Roughening and Groove Formation

The strain concentration described earlier promotes surface roughening around the banded region, ultimately leading to grooving in that area. Figure 11 illustrates the evolving surface profile with increasing straining cycles, highlighting surface undulation up to  $N = 90$  cycles. This local deformation creates a sample-wide biased surface slope, including a protruded left edge, as the system seeks overall equilibrium. Notably, the banded region displays a significantly larger slope, indicative of localized strain that contributes to grooving at its right edge. The magnified view on the left captures the early stage of groove formation at the intersection of the PSB and the surface, where a shallow but distinct groove tip is evident at the right edge of the laddered band. These observations clearly demonstrate that spontaneous substructuring alone can effectively reproduce surface roughening and initiate the formation of groove embryos.

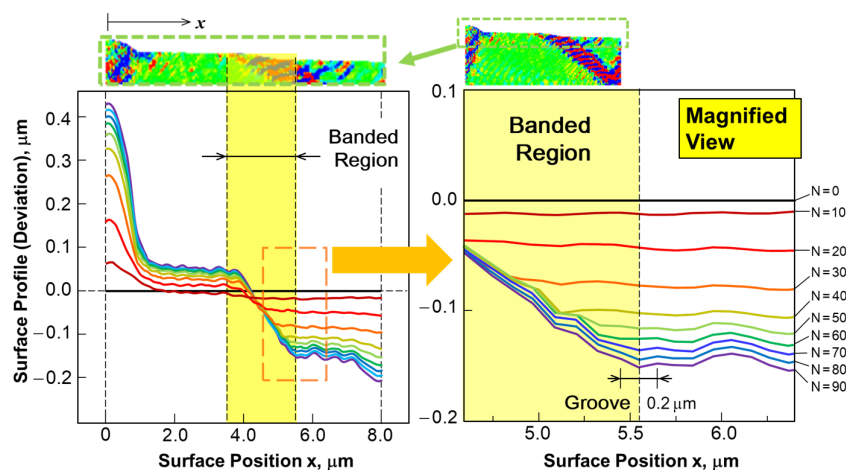


**Figure 11.** Variation in surface profile with straining cycles, accompanied by a magnified view illustrating the evolving groove at the PSB–matrix interface region. The surface region for measuring the profile is outlined by a green dashed box in the inset, while the yellow highlights denote the banded region.

### 5.4. Preliminary Analysis with Vacancy Effect Using a Simplified Model

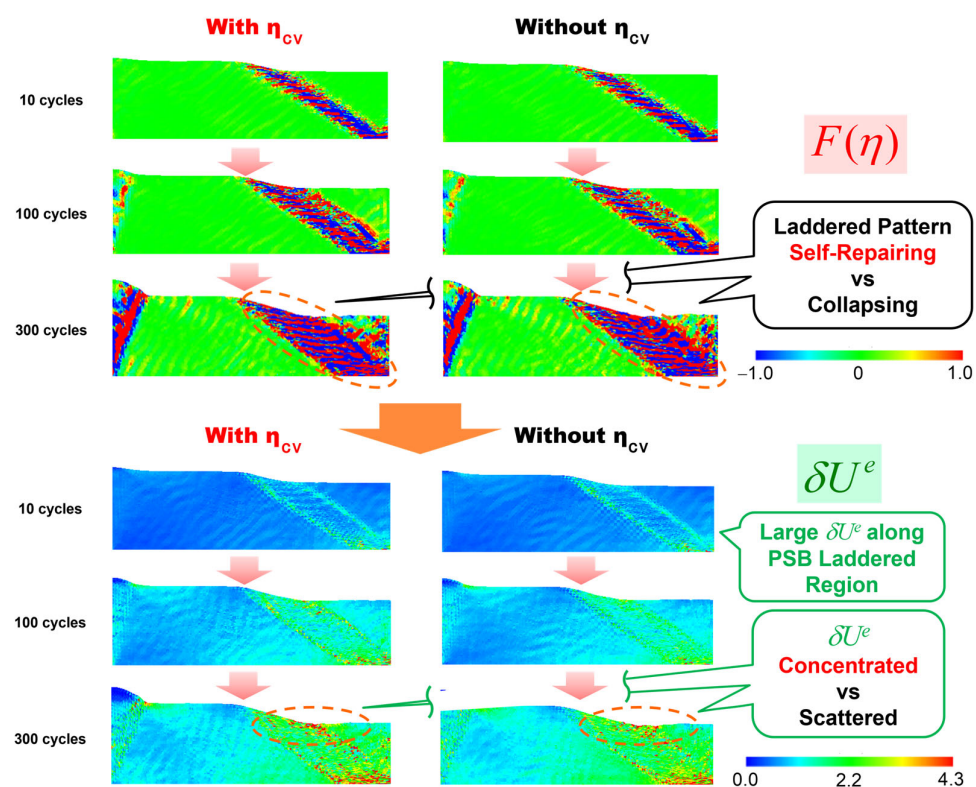
To anticipate the effect of the formed pattern on the subsequent behavior of the PSB and the resulting development of surface undulations, we introduce a simplified model for vacancy formation. This serves as a prelude to the explicit treatments of the vacancy source model coupled with diffusion analysis that will be explored in Part II [69]. Assuming that the gradient of the elastic strain energy attended with the formed ladder pattern can promote vacancy diffusion, combined with the flow-evolutionary law Equation (8), we introduce the following simplified model via the incompatibility term:

$$\eta_{cv} = \kappa_v \delta U^e \quad (22)$$

The idea here is inspired by a systematic series of diffusion analyses described in Appendix D, where the diffusion equation for vacancy concentration is solved against an assumed ladder pattern specified by an a priori elastic strain energy distribution. In these diffusion analyses, diffusion is solely enhanced by the gradient of the elastic strain energy,

which is now reflected through the incompatibility term  $F(\eta_{cv})$  in the present analysis. We incorporate this term into the original  $F(\eta)$  in the hardening ratio  $Q_{\alpha\beta}$ , anticipating a positive contribution to groove formation and further growth.

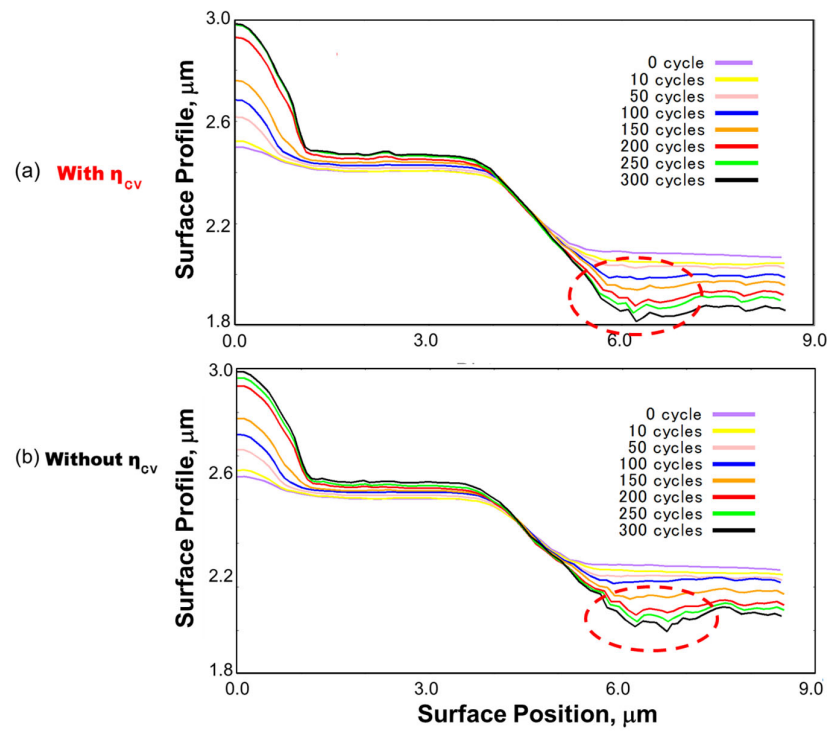
Figure 12 presents a comparison of incompatibility contours (top) and the corresponding elastic strain energy fluctuations (bottom) ( $F(\eta)$  and  $\delta U^e$ ) to assess the effect of the simplified vacancy model on the evolution of laddered patterns in the PSB region. In the absence of the vacancy model (right row), the laddered pattern tends to collapse partially along the righthand side edge of PSBs as straining cycles progress, as indicated by the incompatibility contours. This ultimately results in a relatively scattered distribution of  $\delta U^e$  around the PSB edge on the sample surface. In contrast, incorporating the vacancy model (left row) appears to stabilize the pattern, leading to a concentration of  $\delta U^e$ . We anticipate that this contribution to elastic strain energy fluctuations will foster the healthy development of surface grooves.



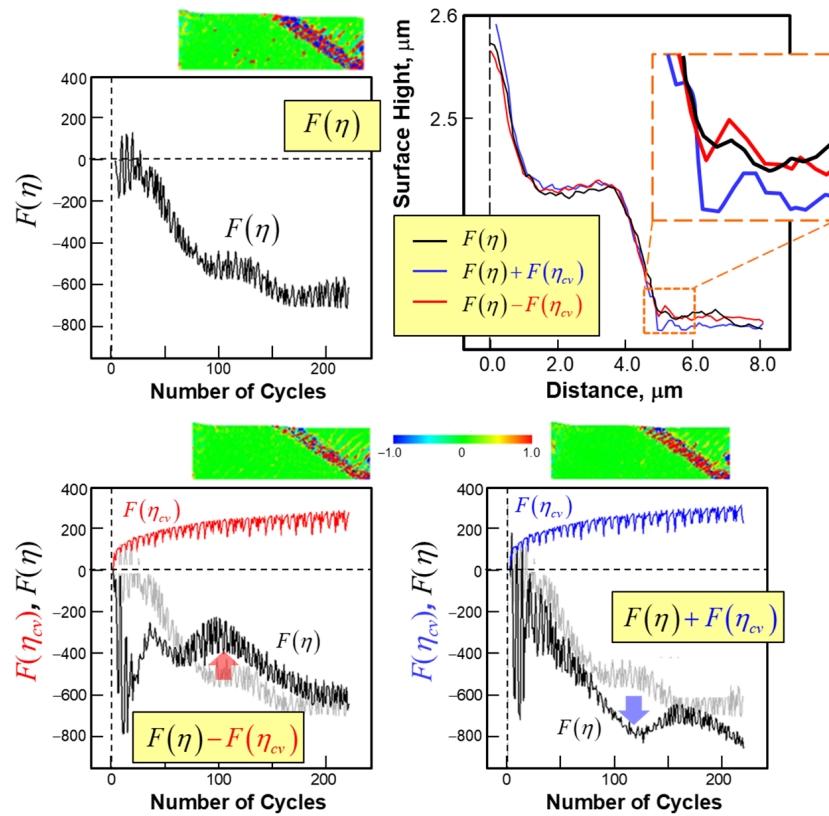
**Figure 12.** Effect of the simplified vacancy model on the evolution of incompatibility and the associated elastic strain energy fluctuations.

Figure 12 compares the evolution of surface profiles with and without the contribution of  $\eta_{cv}$ . The inclusion of  $\eta_{cv}$  leads to the formation of a single groove, whereas its absence results in a splitting of the groove peaks, becoming evident after 200 straining cycles. This behavior corresponds to the concentrated and diffused strain energy distributions seen in Figure 11.

To further investigate the role of  $\eta_{cv}$  in the final surface grooving, we examine the individual variations of the incompatibility terms  $F(\eta)$  and  $F(\eta_{cv})$  with respect to straining cycles in Figure 13. The term  $F(\eta_{cv})$  itself increases parabolically with the number of cycles while exhibiting periodic oscillations, simply reflecting the applied cyclic straining. Adding  $F(\eta_{cv})$  significantly increases the overall variation of  $F(\eta)$  in the negative direction (bottom right), while subtracting it leads to a mild decrease in the overall change (bottom left). This upward trend in  $F(\eta)$  enhances local deformation, resulting in a converging and sharpened groove, as confirmed by the final surface profile displayed at the top right of Figure 14.



**Figure 13.** Evolution of surface grooving as a function of straining cycles, comparing scenarios with and without the simplified vacancy model. The influence of the vacancy model on the development of surface features over time is highlighted. Groove regions in the final surface profiles are marked by red dashed circles for clarity.



**Figure 14.** Variation of incompatibility terms with the number of cycles, illustrating the effect of the simplified vacancy model on surface grooving.

These results clearly demonstrate that the addition of  $F(\eta_{cv})$  positively promotes grooving by significantly sharpening and deepening the groove profile, as anticipated. This ultimately leads to an accumulation of strain energy at the right edge of the PSB-sample surface intersection, whereas, in the absence of this term, the elastic strain energy tends to diffuse. We will utilize the final surface profile (b) for restart analyses to be conducted in Part II of the present study [69].

### 5.5. Discussion and Future Scope

In this study, we have successfully demonstrated that the FTMP-incorporated CP-FEM simulation can effectively reproduce the empirically observed ladder morphology and the PSB. Moreover, this simulation adeptly captures the dynamics of surface roughening and the eventual formation of grooves, even in the absence of vacancy formation and diffusion. These findings underscore the significance of the incompatibility tensor-based underlying degrees of freedom, which possess a remarkable capability to reproduce dislocation substructures, features that are often lacking in conventional CP-FEM approaches. This advancement not only helps enhance our understanding of PSB ladder patterning but also opens new avenues for further exploring the complex interplay of microstructural features that dictate the eventual crack initiation process, as will be extended in Part II [69].

The current simulation can be seamlessly extended to multi-grain scenarios, as demonstrated in Figure 15. This figure showcases three preliminary examples featuring single slip-oriented grains located in (a) the upper half, (b) the surface-facing grain, and (c) the central grain. In each case, we observe similar PSB ladder formations exclusively in the single slip oriented grain, as observed previously, which intriguingly terminate at the grain boundaries. These results underscore the potential for expanding the present study to polycrystalline simulations, highlighting the versatility and applicability of our approach.

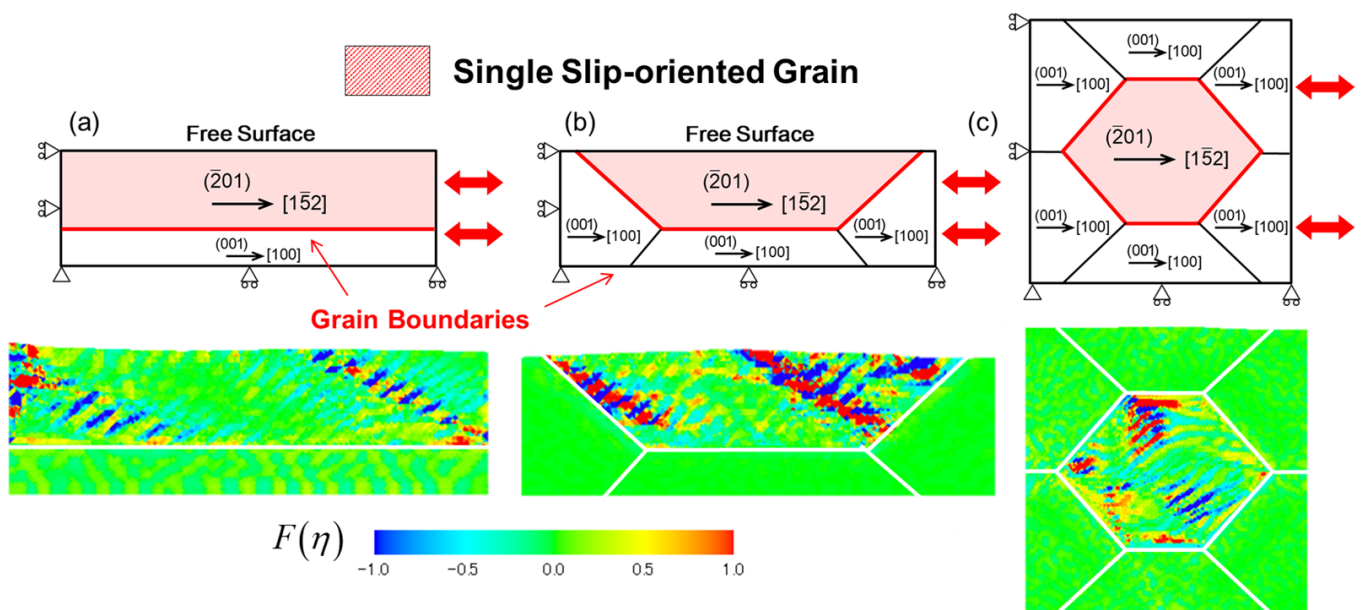


**Figure 15.** Examples of extended simulation results showing incompatibility contours in multi-grain scenarios featuring grain boundaries, featuring a single slip-oriented grain in (a) the upper half, (b) the surface-facing grain, and (c) the central grain of the samples, respectively.

## 6. Conclusions

In this study, we first demonstrate that PSB ladder substructuring during cyclic straining can be effectively reproduced through simple deformation analyses, showcasing the predictive capability of the FTMP framework. Notably, this achievement does not require any ad hoc models, intricate mathematical formulations, or elaborate finite element discretization. This reinforces our confidence in the practical feasibility of computational

modeling for fatigue crack initiation processes and supports our advancement to the next stage of research without relying on complex modeling approaches.

Furthermore, the FTMP-incorporated CP-FEM simulation not only replicates the empirically observed ladder morphology and PSBs with satisfactory accuracy, but also adeptly simulates surface roughening and eventual grooving, independent of vacancy formation and diffusion. This highlights the crucial role of ladder morphology in these processes and lays the groundwork for further investigations into the effects of vacancy formation through explicit diffusion analyses in Part II [69]. These advancements stem from the incompatibility of tensor-based underlying degrees of freedom, which offer exceptional capabilities in modeling dislocation substructures often overlooked by conventional CP-FEM approaches. Thus, the robustness of the FTMP framework is validated, positioning it as a transformative tool in materials science and paving the way for deeper insights into slip band-fatigue crack transition.

**Author Contributions:** Conceptualization, T.H.; methodology, T.H.; software, X.Y. and T.H.; validation, T.H.; formal analysis, X.Y.; investigation, X.Y.; resources, X.Y. and T.H.; data curation, X.Y. and T.H.; writing—original draft preparation, X.Y. and T.H.; writing—review and editing, T.H.; visualization, X.Y. and T.H.; supervision, X.Y. and T.H.; project administration, T.H.; funding acquisition, T.H. All authors have read and agreed to the published version of the manuscript.

**Funding:** This research was partially supported by the Air Force Office of Scientific Research (AFOSR) under grant number FA4869-07-1-4101 and by JSPS KAKENHI for Scientific Research (C) under grant number 21560092.

**Data Availability Statement:** The original contributions presented in the study are included in the article, further inquiries can be directed to the corresponding author.

**Conflicts of Interest:** The authors declare no conflict of interest.

## Appendix A. Cartesian Coordinate Expressions of Dislocation Density Tensor and Incompatibility Tensor and Extended 4D Spacetime Components

The explicit expressions of the dislocation density tensor and the incompatibility tensor for 3D in terms of plastic distortion tensor  $\beta_{ij}^p$  and the plastic strain tensor  $\varepsilon_{ij}^p$  are given as follows:

$$\begin{bmatrix} \alpha_{11} & \alpha_{12} & \alpha_{13} \\ \alpha_{21} & \alpha_{22} & \alpha_{23} \\ \alpha_{31} & \alpha_{32} & \alpha_{33} \end{bmatrix} = - \begin{bmatrix} \partial_2 \beta_{31}^p - \partial_3 \beta_{21}^p & \partial_2 \beta_{32}^p - \partial_3 \beta_{22}^p & \partial_2 \beta_{33}^p - \partial_3 \beta_{23}^p \\ \partial_3 \beta_{11}^p - \partial_1 \beta_{31}^p & \partial_3 \beta_{12}^p - \partial_1 \beta_{32}^p & \partial_3 \beta_{13}^p - \partial_1 \beta_{33}^p \\ \partial_1 \beta_{21}^p - \partial_2 \beta_{11}^p & \partial_1 \beta_{22}^p - \partial_2 \beta_{12}^p & \partial_1 \beta_{23}^p - \partial_2 \beta_{13}^p \end{bmatrix} \quad (A1)$$

$$\begin{bmatrix} \eta_{11} & \eta_{12} & \eta_{13} \\ & \eta_{22} & \eta_{23} \\ Sym & & \eta_{33} \end{bmatrix} = \begin{bmatrix} (\partial_2^2 \varepsilon_{33}^p + \partial_3^2 \varepsilon_{22}^p) - 2\partial_2 \partial_3 \varepsilon_{23}^p & \partial_3 (\partial_1 \varepsilon_{23}^p + \partial_2 \varepsilon_{31}^p - \partial_3 \varepsilon_{12}^p) - \partial_1 \partial_2 \varepsilon_{33}^p & \partial_2 (\partial_3 \varepsilon_{12}^p + \partial_1 \varepsilon_{23}^p - \partial_2 \varepsilon_{31}^p) - \partial_3 \partial_1 \varepsilon_{22}^p \\ & (\partial_3^2 \varepsilon_{11}^p + \partial_1^2 \varepsilon_{33}^p) - 2\partial_3 \partial_1 \varepsilon_{31}^p & \partial_1 (\partial_2 \varepsilon_{31}^p + \partial_3 \varepsilon_{12}^p - \partial_1 \varepsilon_{23}^p) - \partial_2 \partial_3 \varepsilon_{11}^p \\ & & (\partial_1^2 \varepsilon_{22}^p + \partial_2^2 \varepsilon_{11}^p) - 2\partial_1 \partial_2 \varepsilon_{12}^p \end{bmatrix} \quad (A2)$$

For extended 4D spacetime definition for the incompatibility tensor, we have

$$\eta_{ij} = \epsilon_{iklp} \epsilon_{jmn} \partial_k \partial_m \varepsilon_{ln}^p \quad (A3)$$

The pure temporal component  $\eta_{44}$  is obtained by putting  $(i, j) = (4, 4)$  in Equation (A3).

$$\eta_{44} = \epsilon_{4klp} \epsilon_{4mnp} \partial_k \partial_m \varepsilon_{ln}^p \quad (A4)$$

While the dummy index  $p$  runs from 1 to 3, the alternating symbol is restricted to three cases, as given by

$$\eta_{44} = \epsilon_{4kl1} \epsilon_{4mn1} \partial_k \partial_m \epsilon_{ln}^p + \epsilon_{4kl2} \epsilon_{4mn2} \partial_k \partial_m \epsilon_{ln}^p + \epsilon_{4kl3} \epsilon_{4mn3} \partial_k \partial_m \epsilon_{ln}^p \tag{A5}$$

The first term on the right-hand side, for example, is

$$\begin{aligned} (\text{Eq. (A4')})_{1st} &= \epsilon_{4kl1} \epsilon_{4mn1} \partial_k \partial_m \epsilon_{ln}^p \\ &= \partial_2^2 \epsilon_{33}^p + \partial_3^2 \epsilon_{22}^p - 2\partial_2 \partial_3 \epsilon_{23}^p \end{aligned} \tag{A6}$$

which coincides with the  $\eta_{11}$  component in Equation (A2). Similarly, the second and third terms correspond to  $\eta_{22}$  and  $\eta_{33}$ , respectively. Therefore, we conclude that the equality is

$$\eta_{44} = \eta_{KK} \tag{A7}$$

A spatio-temporal mixed component,  $\eta_{14}$  for example, by setting  $(i j) = (1,4)$  in Equation (A3), becomes

$$\eta_{14} = \epsilon_{1klp} \epsilon_{4mnp} \partial_k \partial_m \epsilon_{ln}^p \tag{A8}$$

Similar to the above, while the dummy index  $p$  can take values 2 or 3, the alternating symbol is restricted to two cases, as given by

$$\eta_{14} = \epsilon_{1kl2} \epsilon_{4mn2} \partial_k \partial_m \epsilon_{ln}^p + \epsilon_{1kl3} \epsilon_{4mn3} \partial_k \partial_m \epsilon_{ln}^p \tag{A9}$$

In this case, the first term on the right-hand side is further decomposed into four terms as

$$\begin{aligned} (\text{Eq. (A9)})_{1st} &= \epsilon_{1kl2} \epsilon_{4mn2} \partial_k \partial_m \epsilon_{ln}^p \\ &= \epsilon_{1342} \epsilon_{4132} \partial_k \partial_m \epsilon_{ln}^p + \epsilon_{1342} \epsilon_{4312} \partial_k \partial_m \epsilon_{ln}^p \\ &\quad + \epsilon_{1432} \epsilon_{4312} \partial_k \partial_m \epsilon_{ln}^p + \epsilon_{1432} \epsilon_{4132} \partial_k \partial_m \epsilon_{ln}^p \\ &= \partial_3 \partial_1 \epsilon_{43}^p - \partial_3 \partial_3 \epsilon_{41}^p + \partial_4 \partial_3 \epsilon_{31}^p - \partial_4 \partial_1 \epsilon_{33}^p \\ &= \partial_3 (\partial_1 \epsilon_{43}^p - \partial_3 \epsilon_{41}^p) + \partial_3 \partial_4 \epsilon_{13}^p - \partial_4 \partial_1 \epsilon_{33}^p \end{aligned} \tag{A10}$$

Noticing that  $\partial_1 \epsilon_{43}^p - \partial_3 \epsilon_{41}^p = \partial_1 \dot{u}_3^p - \partial_3 \dot{u}_1^p = \dot{\omega}_{13}^p$ ,  $\partial_4 \partial_3 \epsilon_{13}^p = \partial_3 \dot{\epsilon}_{13}^p$ , and  $\partial_4 \partial_1 \epsilon_{33}^p = \partial_1 \dot{\epsilon}_{33}^p = \partial_1 \dot{\beta}_{33}^p$ , along with the definition of  $\alpha_{23}$  in Equation (A1), we can rewrite the above as

$$\begin{aligned} (\text{Eq. (A9)})_{1st} &= \partial_3 (\dot{\omega}_{13}^p + \dot{\epsilon}_{13}^p) - \partial_1 \dot{\beta}_{33}^p \\ &= \partial_3 \dot{\beta}_{13}^p - \partial_1 \dot{\beta}_{33}^p \\ &= -\dot{\alpha}_{23} \end{aligned} \tag{A11}$$

Similarly, for the second term on the right-hand side, we have

$$\begin{aligned} (\text{Eq. A9})_{2nd} &= \partial_2 (\dot{\omega}_{12}^p + \dot{\epsilon}_{12}^p) - \partial_1 \dot{\beta}_{22}^p \\ &= -(\partial_1 \dot{\beta}_{22}^p - \partial_2 \dot{\beta}_{12}^p) \\ &= \dot{\alpha}_{32} \end{aligned} \tag{A12}$$

Combining the above results (Equations (A11) and (A12)), we ultimately obtain

$$\eta_{14} = -(\dot{\alpha}_{23} - \dot{\alpha}_{32}) \tag{A13}$$

This represents a skew-symmetric part of the edge component in the dislocation density tensor from Equation (A1). The other spatio-temporal mixed components are given by

$$\eta_{24} = -(\dot{\alpha}_{31} - \dot{\alpha}_{13}) \text{ and } \eta_{34} = -(\dot{\alpha}_{12} - \dot{\alpha}_{21}) \tag{A14}$$

In general, we express them collectively as

$$\eta_{A4} = -(\dot{\alpha}_{BC} - \dot{\alpha}_{CB}) = -2(\alpha_{BC})_{skew} \quad (A15)$$

## Appendix B. Historical Context and Derivation of the Flow-Evolutionary Law (FEL)

The current approach in FTMP insists that the flow-evolutionary law (Equation (4)) is based on the idea that “the incompatible displacement (i.e., displacement indeterminacy due to curvature) is driven by a configurational force (e.g., inhomogeneity or singularity), represented as a conserved quantity corresponding to the energy-momentum tensor, based on Noether’s theorem” in 4D spacetime [72]. To this end, the incompatibility tensor is extended to 4D spacetime in [57]. Since curvature in crystalline space is geometrical and lacks an inherent driving force, it must be linked to a physical quantity that provides the driving force for its evolution. The flow-evolutionary law, proposed as a working hypothesis within the current FTMP, serves as a candidate for governing this process.

Historically, the incompatibility tensor has been used to derive stress fields related to dislocation density, as discussed by Kröner [73,74]. However, in the current context, we interpret this tensor as a continuum mechanics representation of the curvature tensor of the crystalline space, reflecting the classification of imperfections in terms of torsion and curvature based on differential geometry. This idea, first proposed by Kazuo Kondo in the 1950s as “non-Riemannian plasticity” [75], predates and is independent of the work by Bilby [76], Kröner, and Eshelby [77]. While Bilby acknowledged the relationship between torsion and dislocations, he dismissed the role of curvature, claiming that curvature changes the material vector along parallel displacement, thus no longer representing the crystal. Kondo countered this by stating that if torsion causes closure failure (e.g., in the Burgers circuit), it no longer represents a continuum. This suggests that Bilby’s argument is incomplete within the continuum mechanics framework. Additionally, Bilby’s work was influenced by E. Cartan’s 1923 concept of torsion in spaces with asymmetric connections [78].

The incompatibility tensor coincides with Einstein’s tensor in general relativity. Both satisfy the divergence-free condition, a key characteristic shared with the energy-momentum tensor, which appears on the right-hand side of Einstein’s field equations for gravity. This connection underscores the mathematical parallels between continuum mechanics and general relativity, reinforcing the idea that the incompatibility tensor is essential for understanding material imperfections in a broader geometric context.

The energy-momentum tensor itself traces back to Emmy Noether’s work in classical field theory [72], with its generalized formulation later published by Landau and Lifshitz in *The Classical Theory of Fields* (1923), Section 33 [79]. For an arbitrary field variable  $\varphi_e^i$ , the energy momentum tensor  $T_{ab}$  is given as

$$T_{ab} = \frac{\partial \mathcal{L}}{\partial(\partial_a \varphi_{ie})} \partial_b \varphi_{ie} - \delta_{ab} \mathcal{L} \quad (A16)$$

where  $\mathcal{L}$  represents the Lagrangian density of the system under consideration, and the indices  $a, b$  run from 1 to 4, with time as the fourth dimension. For a deformation field, we regard  $\varphi_{ij} = \partial_i u_j = \beta_{ij}$  as the distortion tensor. When focussing solely on the spatial components (i.e.,  $a, b, \dots = A, B, \dots$ ), this expression reduces to that presented by Eshelby [80,81]. Assuming elasticity with  $C_{ABCD}^e$  as the elastic stiffness tensor,  $\mathcal{L} = \frac{1}{2} \rho_0 \beta_{i4} \delta_{ij} \beta_{j4} - \frac{1}{2} C_{ABCD}^e \varepsilon_{AB} \varepsilon_{CD}$ , and one obtains

$$T_{AB} = -\sigma_{Ai} \beta_{Bi} + \delta_{AB} \mathcal{W} \quad (A17)$$

This is precisely the expression derived by Eshelby in his 1975 paper [81] as  $P_{AB}$ . The pure temporal component, i.e.,  $(a,b) = (4,4)$ , on the other hand, corresponds to the total energy of the system

$$T_{44} = \frac{1}{2} \rho_0 \beta_{i4} \delta_{ij} \beta_{j4} + \frac{1}{2} C_{ABCD}^e \varepsilon_{AB} \varepsilon_{CD} = \mathcal{H} \quad (A18)$$

where  $\mathcal{H} \equiv \mathcal{K} + \mathcal{W}$  represents the Hamiltonian density. In the present study, the potential energy  $\mathcal{W}$  is interpreted as the elastic strain energy  $U^e$ . Eshelby's work [81,82], particularly his 1975 paper [81], acknowledged Noether's discovery but derived the tensor  $P_{AB}$  from a mechanics perspective. While Eshelby's contribution to continuum solid mechanics was significant, his formulation is essentially the spatial part of the energy-momentum tensor defined in 4D spacetime, coinciding with Equation (A17), as shown above.

Parenthetically, a similar attempt is found in Epstein et al. [82], where the energy-momentum tensor (expressed as the Eshelby stress in their context) is interlinked with geometrical quantities. However, they ultimately arrived at a final form (referred to as the "full balance law" in their terminology) [83] involving the torsion tensor, rather than the curvature tensor.

### Appendix C. Extended Divergence-Free Condition of the Incompatibility Tensor in 4D Spacetime

In this section, we derive Equation (11) from the divergence-free condition given by Equation (9). When extending the definition of the incompatibility tensor into 4D spacetime, the conservation law represented by the divergence-free condition must also be extended accordingly. The condition is given by

$$\begin{aligned} \frac{\partial \eta_{ab}}{\partial x^a} = \partial_a \eta_{ab} = 0 &\Rightarrow \frac{\partial \eta_{44}}{\partial x^4} + \frac{\partial \eta_{A4}}{\partial x^A} = 0 \\ &\Leftrightarrow \dot{\eta}_{KK} = -div \eta_{A4} \end{aligned} \quad (A19)$$

where Equation (A7) is used. The physical interpretation of this relationship becomes clear when considered in its integral form as

$$\begin{aligned} \frac{\partial}{\partial t} \int_v \eta_{KK} dv &= - \int_v \frac{\partial \eta_{A4}}{\partial x^A} dv \\ &= - \int_a n_A \eta_{A4} da \end{aligned} \quad (A20)$$

This indicates that the rate of change of incompatibility within the volume element  $dv$  is equivalent to the flux of incompatibility  $\eta_{A4}$  across the boundary surface  $da_A$  (the  $x^A$ -surface). Combining the results from Equation (A15) in Appendix A, we ultimately arrive at the important relationship between the rate of incompatibility and the edge dislocation flux.

$$\dot{\eta}_{KK} = div(\alpha_{BC} - \alpha_{CB}) \quad (A21)$$

Thus, we derive Equation (11).

### Appendix D. Preparatory Diffusion Analysis on PSB-Laddered Sample

At the preparatory stage, we conducted pure diffusion analyses, assuming a PSB-laddered strain energy distribution a priori, to examine the effects of laddered morphology on vacancy diffusion and the resulting surface recession, including the wall position relative to the sample surface. This was achieved by solving the diffusion equation employed by Repetto and Ortiz [51] using the finite difference method (FDM). The analytical model and the key results are summarized in Figures A1 and A2. The initial vacancy concentration is assumed to be uniformly distributed across the sample, with an equilibrium value of  $c_{veq} = \exp(-\Delta G_v/kT)$ . Here,  $\Delta G_v$  represents the free energy change per vacancy, approximately 0.9eV for  $\alpha$ -Fe at room temperature, while  $k$  and  $T$  are Boltzmann constant and absolute temperature, respectively. The model considers only the contribution of lattice diffusion, represented by  $D_{lattice} = 1.5 \times 10^{-15} \text{ m}^2/\text{s}$ , while neglecting pipe diffusion. The findings are as follows:

- (i) Insensitivity to the wall position.
- (ii) Wherever vacancies are generated—whether in the channel or wall regions—they first flow into the wall, then out of the wall edges into the PSB–matrix interface, subsequently diffusing toward the surface along that interface.

(iii) Ladder walls play a critical role in developing and enhancing surface grooving; without them, surface recession does not occur.

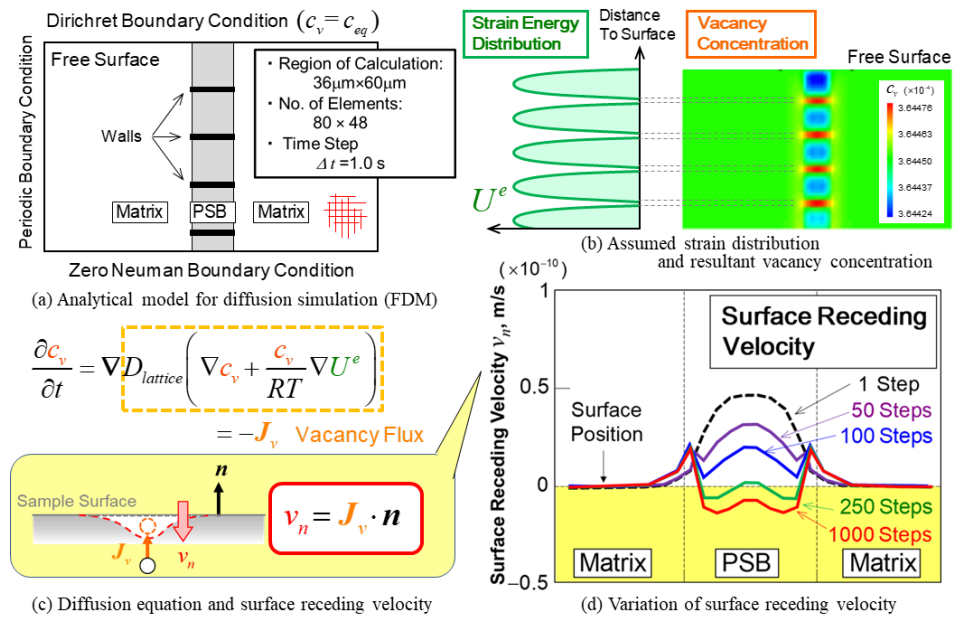


**Figure A1.** Overview of preparatory diffusion analyses using the finite difference method (FDM): (a) analytical model assuming a priori the ladder walls defined by elastic strain energy distribution (b), (c) diffusion equation employed, and (d) resultant surface receding velocity distribution via vacancy flux indicated in (c).

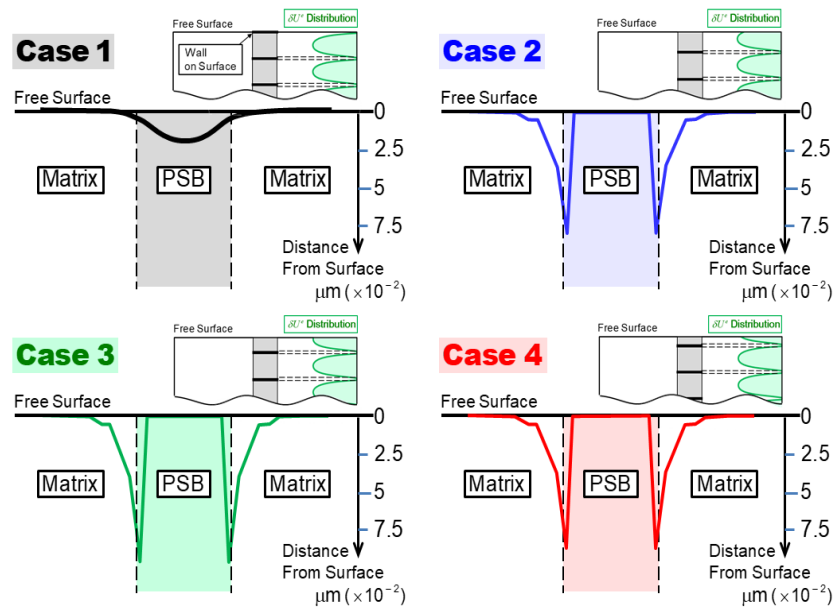


**Figure A2.** Simulated surface profiles at  $t = 1000$  simulation steps, comparing the effect of ladder wall position relative to the sample surface for Cases 1 through 4.

**References**

1. Thompson, N.; Wadsworth, N.J.; Louat, N. The Origin of Fatigue Fracture in Copper. *Philos. Mag.* **1956**, *1*, 113–126. [CrossRef]
2. Woods, P.J. Low-amplitude Fatigue of Copper and Copper-5 at.% Aluminium Single Crystals. *Philos. Mag.* **1973**, *28*, 155–191. [CrossRef]
3. Polák, J. On the Role of Point Defects in Fatigue Crack Initiation. *Mater. Sci.* **1987**, *92*, 71–80. [CrossRef]

4. Polák, J.; Petreenc, M.; Man, J. Dislocation Structure and Surface Relief in Fatigued Metals. *Mater. Sci. A* **2005**, *400–401*, 405–408. [[CrossRef](#)]
5. Polák, J. Production, Annihilation and Migration of Point Defects in Cyclic Straining. *Materialia* **2020**, *14*, 100938. [[CrossRef](#)]
6. Polák, J. Role of Persistent Slip Bands and Persistent Slip Markings in Fatigue Crack Initiation in Polycrystals. *Crystals* **2023**, *13*, 220. [[CrossRef](#)]
7. Essmann, U.; Mughrabi, H. Annihilation of Dislocations during Tensile and Cyclic Deformation and Limits of Dislocation Densities. *Philos. Mag. A* **1979**, *40*, 731–756. [[CrossRef](#)]
8. Essmann, U. Irreversibility of cyclic slip in persistent slip bands of fatigued pure fcc metals. *Philos. Mag. A* **1982**, *45*, 171–190. [[CrossRef](#)]
9. Jones, W.J.D.; Dover, W.D. Enhanced Diffusion Rates during the Fatigue of Metals. *Nature* **1966**, *209*, 704. [[CrossRef](#)]
10. Robergre, R.; Herman, H. Fatigue—Generation of Vacancies. *Nature* **1966**, *211*, 178–179. [[CrossRef](#)]
11. Zhang, X.; Stinville, J.-C.; Pollock, T.M.; Dunne, F.P.E. Crystallography and Elastic Anisotropy in Fatigue Crack Nucleation at Nickel Alloy Twin Boundaries. *J. Mech. Phys. Solids* **2021**, *155*, 104538. [[CrossRef](#)]
12. Li, L.; Zhang, Z.; Zhang, P.; Zhang, Z. A Review on the Fatigue Cracking of Twin Boundaries: Crystallographic Orientation and Stacking Fault Energy. *Prog. Mater. Sci.* **2023**, *131*, 101011. [[CrossRef](#)]
13. Zhu, G.; Kang, B.; Zhu, M.-L.; Xuan, F.-Z. Quantitative Assessment of Microstructural Damage for Interior Crack Initiation and High Cycle Fatigue Life Modeling. *Mater. Sci. Eng. A* **2024**, *904*, 146707. [[CrossRef](#)]
14. Chen, B.; Jiang, J.; Dunne, F.P.E. Is Stored Energy Density the Primary Meso-Scale Mechanistic Driver for Fatigue Crack Nucleation? *Int. J. Plast.* **2018**, *101*, 213–229. [[CrossRef](#)]
15. Pandey, V.B.; Singh, I.V.; Mishra, B.K.; Ahmad, S.; Venugopal Rao, A.; Kumar, V. A New Framework Based on Continuum Damage Mechanics and XFEM for High Cycle Fatigue Crack Growth Simulations. *Eng. Fract. Mech.* **2019**, *206*, 172–200. [[CrossRef](#)]
16. Borges, M.F.; Neto, D.M.; Antunes, F.V. Numerical Simulation of Fatigue Crack Growth Based on Accumulated Plastic Strain. *Theor. Appl. Fract. Mech.* **2020**, *108*, 102676. [[CrossRef](#)]
17. Pan, Y.; Wu, P.; Fan, S.; Peng, X.; Chen, Z. Peridynamic Simulation of Fatigue Crack Growth in Porous Materials. *Eng. Fract. Mech.* **2024**, *300*, 109984. [[CrossRef](#)]
18. Zhou, H.; Suzuki, Y.; Kinefuchi, M.; Schmauder, S.; Dogahe, K.; Shibamura, K. Bridging Strategy between Microscopic and Macroscopic Crack Growth Simulations to Predict Fatigue Strength of Steels. *Int. J. Fatigue* **2023**, *168*, 107386. [[CrossRef](#)]
19. Babu Rao, V.; Phung, B.R.; Johnsson, B.T.; Spear, A.D. Statistical Analysis of Microstructurally Small Fatigue Crack Growth in Three-Dimensional Polycrystals Based on High-Fidelity Numerical Simulations. *Eng. Fract. Mech.* **2024**, *307*, 110282. [[CrossRef](#)]
20. Sun, B.; Xu, Y.-L.; Li, Z. Multi-Scale Fatigue Model and Image-Based Simulation of Collective Short Cracks Evolution Process. *Comput. Mater. Sci.* **2016**, *117*, 24–32. [[CrossRef](#)]
21. Zhao, Z.; Ramesh, M.; Raabe, D.; Cuitiño, A.M.; Radovitzky, R. Investigation of Three-Dimensional Aspects of Grain-Scale Plastic Surface Deformation of an Aluminum Oligocrystal. *Int. J. Plast.* **2008**, *24*, 2278–2297. [[CrossRef](#)]
22. Grilli, N.; Janssens, K.G.F.; Nellessen, J.; Sandlöbes, S.; Raabe, D. Multiple Slip Dislocation Patterning in a Dislocation-Based Crystal Plasticity Finite Element Method. *Int. J. Plast.* **2018**, *100*, 104–121. [[CrossRef](#)]
23. Radi, A.; Sajadifar, S.; Seyedmohammadi, S.V.; Krochmal, M.; Bolender, A.; Wegener, T.; Niendorf, T.; Yapici, G.G. On the Low-Cycle Fatigue Behavior of a Multi-Phase High Entropy Alloy with Enhanced Plasticity. *Int. J. Fatigue* **2023**, *173*, 107678. [[CrossRef](#)]
24. Prastiti, N.G.; Xu, Y.; Balint, D.S.; Dunne, F.P.E. Discrete Dislocation, Crystal Plasticity and Experimental Studies of Fatigue Crack Nucleation in Single-Crystal Nickel. *Int. J. Plast.* **2020**, *126*, 102615. [[CrossRef](#)]
25. Irastorza-Landa, A.; Van Swygenhoven, H.; Van Petegem, S.; Grilli, N.; Bollhalder, A.; Brandstetter, S.; Grolimund, D. Following Dislocation Patterning during Fatigue. *Acta Mater.* **2016**, *112*, 184–193. [[CrossRef](#)]
26. Zhai, H.; Jiang, J.; Zhang, W.; Zhang, Q.; Ma, X.; Wang, S.; Li, Z.; Qiu, W.; Xiao, C.; Lin, H. Microstructure Sensitivity of the Low Cycle Fatigue Crack Initiation Mechanisms for the Al<sub>0.3</sub>CoCrFeNi High Entropy Alloy: In-Situ SEM Study and Crystal Plasticity Simulation. *Int. J. Fatigue* **2023**, *176*, 107871. [[CrossRef](#)]
27. Kubin, L.; Sauzay, M. Persistent Slip Bands: Similitude and Its Consequences. *Acta Mater.* **2016**, *104*, 295–302. [[CrossRef](#)]
28. Hussein, A.M.; El-Awady, J.A. Quantifying Dislocation Microstructure Evolution and Cyclic Hardening in Fatigued Face-Centered Cubic Single Crystals. *J. Mech. Phys. Solids* **2016**, *91*, 126–144. [[CrossRef](#)]
29. Heinrich, C.; Sundararaghavan, V. A method to predict fatigue crack initiation in metals using dislocation dynamics. *Corros. Rev.* **2017**, *35*, 325–341. [[CrossRef](#)]
30. Wang, Y.; Li, J. Phase Field Modeling of Defects and Deformation. *Acta Mater.* **2010**, *58*, 1212–1235. [[CrossRef](#)]
31. Xue, F.; Cheng, T.-L.; Lei, Y.; Wen, Y.-H. Phase-Field Modeling of Crack Growth under Coupled Creep-Fatigue. *Int. J. Fatigue* **2024**, *189*, 108577. [[CrossRef](#)]
32. Sangid, M.D. The Physics of Fatigue Crack Initiation. *Int. J. Fatigue* **2013**, *57*, 58–72. [[CrossRef](#)]
33. Lukas, P.; Klesnil, M.; Fiedler, R. Plastic Zone Around the Propagating Fatigue Crack. *Philos. Mag.* **1969**, *18*, 799–805. [[CrossRef](#)]
34. Grosskreutz, J.C.; Shaw, G.G. Microstructures at the Tips of Growing Fatigue Cracks in Aluminum Alloys. In *Fatigue Crack Propagation*; ASTM International: West Conshohocken, PA, USA, 1967; Volume 415, pp. 226–243. [[CrossRef](#)]
35. Wilkins, M.A.; Smith, G.C. Dislocation Structures Near a Propagating Fatigue Crack in an Al 12% mg Alloy. *Acta Metall.* **1970**, *18*, 1035–1043. [[CrossRef](#)]

36. Mughrabi, H. Dislocation Wall and Cell Structures and Long-Range Internal Stresses in Deformed Metal Crystals. *Acta Metall.* **1983**, *31*, 1367–1379. [[CrossRef](#)]
37. Mughrabi, H.; Ungar, T.; Kienle, W.; Wilkens, M. Long-Range Internal Stress and Asymmetric X-Ray Line Broadening in Tensile Deformed [001]-Oriented Copper Single Crystals. *Philos. Mag. A* **1986**, *53*, 793–813. [[CrossRef](#)]
38. Mughrabi, H.; Ackerman, F.; Herz, K. Persistent Slip Bands in Fatigued Face-Centered and Body-Centered Cubic Metals. In *Fatigue Mechanics*; Special Technical Publication 675; Long, J., Ed.; American Society for Testing and Materials (ASTM): West Conshohocken, PA, USA, 1979; pp. 69–105. [[CrossRef](#)]
39. Bao-Tong, M.; Laird, C. Overview of Fatigue Behavior in Copper Single Crystals—I. Surface Morphology and Stage I Crack Initiation Sites for Tests at Constant Strain Amplitude. *Acta Metall.* **1989**, *37*, 325–336. [[CrossRef](#)]
40. Essmann, U.; Gosele, U.; Mughrabi, H. A Model of Extrusions and Intrusions in Fatigued Metals. *Philos. Mag. A* **1981**, *44*, 405–426. [[CrossRef](#)]
41. Suresh, S. *Fatigue of Materials*, 2nd ed.; Cambridge University Press: Cambridge, UK, 1998; pp. 53–68. [[CrossRef](#)]
42. Bretschneider, J.; Holste, C.; Kleinert, W. Mechanical Behaviour and Development of Dislocation Arrangements of fcc Single Crystals Fatigued at 77 K. *Mater. Sci. Eng. A* **1995**, *191*, 61–72. [[CrossRef](#)]
43. Li, P.; Li, S.X.; Wang, Z.G.; Zhang, Z.F. Fundamental Factors on Formation Mechanism of Dislocation Arrangements in Cyclically Deformed Fcc Single Crystals. *Prog. Mater. Sci.* **2011**, *56*, 328–377. [[CrossRef](#)]
44. Ghoniem, N.M.; Walgraef, D. *Instabilities and Self-Organization in Materials*; Oxford University Press: Oxford, UK, 2008.
45. Walgraef, D.; Aifantis, E.C. Dislocation Patterning in Fatigued Metals as a Result of Dynamical Instabilities. *J. Appl. Phys.* **1985**, *58*, 688–691. [[CrossRef](#)]
46. Ghoniem, N.M.; Tong, S.-H.; Sun, L.Z. Parametric Dislocation Dynamics: A Thermodynamics-Based Approach to Investigations of Mesoscopic Plastic Deformation. *Phys. Rev. B* **1999**, *61*, 913–927. [[CrossRef](#)]
47. Kubin, L.; Sauzay, M. Persistent slip bands: The bowing and passing model revisited. *Acta Mater.* **2017**, *132*, 517–524. [[CrossRef](#)]
48. Dodaran, M.; Khonsari, M.M.; Shao, S. Critical operating stress of persistent slip bands in Cu. *Comput. Mater. Sci.* **2019**, *165*, 114–120. [[CrossRef](#)]
49. Brown, L.M. Dislocation bowing and passing in persistent slip bands. *Philos. Mag.* **2006**, *86*, 4055–4068. [[CrossRef](#)]
50. El-Awady, J.A.; Ghoniem, N.M.; Mughrabi, H. Dislocation modelling of localized plasticity in persistent slip bands. In Proceedings of the 136th TMS annual meeting and exhibition, Orlando, FL, USA, 25 February–1 March 2007; pp. 23–35. Available online: [https://www.researchgate.net/publication/253348453\\_Dislocation\\_modelling\\_of\\_localized\\_plasticity\\_in\\_persistent\\_slip\\_bands](https://www.researchgate.net/publication/253348453_Dislocation_modelling_of_localized_plasticity_in_persistent_slip_bands) (accessed on 1 January 2007).
51. Repetto, E.; Ortiz, M. A Micromechanical Model of Cyclic Deformation and Fatigue-Crack Nucleation in fcc Single Crystals. *Acta Mater.* **1997**, *45*, 2577–2595. [[CrossRef](#)]
52. Nakai, Y. Evaluation of Fatigue Damage and Fatigue Crack Initiation Process by Means of Atomic-Force Microscopy. *J. Soc. Mater. Sci. Jpn.* **2001**, *50*, 73–81. [[CrossRef](#)]
53. Nakai, Y.; Kusukawa, T. Quantitative Evaluation of Slip-Band Growth and Crack Initiation in Fatigue of 70-30 Brass by Means of Atomic-Force Microscopy. *Trans. Jpn. Soc. Mech. Eng.* **2001**, *67*, 476–482. [[CrossRef](#)]
54. Nakai, Y.; Maeda, K. Observations of fatigue Slip-Band Growth and Crack Initiation in  $\alpha$ -Brass under Cyclic Shear Stresses by Means of Atomic-Force Microscopy. *J. Mater. Sci. Soc. Jpn.* **2003**, *52*, 625–630. [[CrossRef](#)]
55. Hasebe, T. Interaction Fields Based on Incompatibility Tensor in Field Theory of Plasticity-Part I: Theory. *Interact. Multiscale Mech.* **2009**, *2*, 1–14. [[CrossRef](#)]
56. Hasebe, T. Interaction Fields Based on Incompatibility Tensor in Field Theory of Plasticity-Part II: Application. *Interact. Multiscale Mech.* **2009**, *2*, 15–30. [[CrossRef](#)]
57. Hasebe, T.; Sugiyama, M.; Adachi, H.; Fukutani, S.; Iida, M. Modeling and Simulations of Experimentally-Observed Dislocation Substructures Based on Field Theory of Multiscale Plasticity (FTMP) Combined with TEM and EBSD-Wilkinson Method for FCC and BCC Poly/Single Crystals. *Mater. Trans.* **2014**, *55*, 779–787. [[CrossRef](#)]
58. Hasebe, T. Field Theoretical Multiscale Modeling of Polycrystal Plasticity. *Trans. MRS-J* **2004**, *29*, 3619–3624.
59. Hasebe, T. Multiscale Crystal Plasticity Modeling based on Field Theory. *Comput. Model. Eng. Sci.* **2006**, *11*, 145–156. [[CrossRef](#)]
60. Mizutani, K.; Nawa, Y.; Hasebe, T. Kink Modeling and Simulations Based on Field Theory of Multiscale Plasticity (FTMP) Part I: Explicit Kink Model and Double Compression Test. *Mater. Trans.* **2023**, *64*, 785–794. [[CrossRef](#)]
61. Hasebe, T.; Mizutani, K. Kink Modeling and Simulations Based on Field Theory of Multiscale Plasticity (FTMP) Part II: Implicit Kink Model and Scale-Free Treatment. *Mater. Trans.* **2023**, *64*, 795–804. [[CrossRef](#)]
62. Hasebe, T. *Field Theory of Multiscale Plasticity*, 1st ed.; Cambridge University Press: Cambridge, UK, 2024. [[CrossRef](#)]
63. Yokoi, T.; Takahashi, M.; Maruyama, N.; Sugiyama, M. Application of Controlled Cu Nano-Precipitation for Improvement in Fatigue Properties of Steels. *Nippon Steel Tech. Rep.* **2005**, *91*, 49–55.
64. Yokoi, T.; Takahashi, M.; Maruyama, N.; Sugiyama, M. Cyclic Stress Response and Fatigue Behavior of Cu Added Ferritic Steels. *J. Mater. Sci.* **2001**, *36*, 5757–5765. [[CrossRef](#)]
65. Chen, Z.; Kioussis, N.; Ghoniem, N.; Hasebe, T. Lubricant Effect of Copper Nanoclusters on the Dislocation Core in  $\alpha$ -Fe. *Phys. Rev. B* **2008**, *77*, 014103. [[CrossRef](#)]

66. Kondo, K. Non-Riemannian Geometry of Imperfect Crystals from a Macroscopic Viewpoint. In *Memoirs of the Unifying Study of Basic Problems in Engineering and Physical Sciences by Means of Geometry*; Gakujutsu Bunken Fukyu-kai: Tokyo, Japan, 1955; Volume 1, pp. 458–469.
67. Kondo, K. Derivation of the Differential Equations of Yielding from General Variational Criteria in Analogy with General Relativity Theory and an Extension Thereof to Problems involving Critical Temperature. In *Memoirs of the Unifying Study of Basic Problems in Engineering and Physical Sciences by Means of Geometry*; Gakujutsu Bunken Fukyu-kai: Tokyo, Japan, 1962; Volume 3, pp. 215–227.
68. Ashby, B.F. The Deformation of Plastically Non-Homogeneous Materials. *Philos. Mag.* **1970**, *21*, 399–424. [[CrossRef](#)]
69. You, X.; Hasebe, T. Modeling and Simulation of Fatigue Crack Initiation Process Based on Field Theory of Multiscale Plasticity (FTMP) Part II: Modeling Vacancy Formation and Coupling with Diffusion Analysis. *Metals* **2024**, *in press*.
70. Khan, A.S.; Huang, S. *Continuum Theory of Plasticity*; Wiley Interscience: Hoboken, NJ, USA, 1995.
71. Nemat-Nasser, S.; Plasticity, A. *Treatise on Finite Deformation of Heterogeneous Inelastic Materials*; Cambridge University Press: Cambridge, UK, 2004.
72. Noether, E. Invariant Variations Problems. *Math.—Phys. Kl.* **1918**, *2*, 235–257. (English Translation in *Transp. Theory Stat. Phys.* **1991**, *1*, 186–207). [[CrossRef](#)]
73. Kröner, E. *Kontinuumstheorie der Versetzungen und Eigenspannungen*; Ergebnisse der angewandten Mathematik; Springer: Berlin/Heidelberg, Germany, 1958; Volume 5, pp. 1–179.
74. Kröner, E. Allgemeine Kontinuumstheorie der Versetzungen und Eigenspannungen. *Arch. Ration. Mech. Anal.* **1959**, *4*, 273–334. [[CrossRef](#)]
75. Kondo, K. Non-holonomic Geometry of Plasticity and Yielding. In *Memoirs of Unifying Study of Basic Problems in Engineering and Physical Science by Means of Geometry*; Gakujutsu Bunken Fukyu-kai: Tokyo, Japan, 1955; pp. 453–572.
76. Bilby, B.A.; Bollough, R.; Smith, E. Continuous Distributions of Dislocations: A New Application of the Methods of Non-Riemannian Geometry. *Proc. Roy. Soc. A* **1955**, *231*, 263–273. [[CrossRef](#)]
77. de Wit, R. The Continuum Theory of Stationary Dislocations. *Solid State Phys.* **1960**, *10*, 249–292. [[CrossRef](#)]
78. Cartan, E. Sur les variétés à connexion affine et la théorie de la relativité généralisée (première partie). *Ann. Sci. L'école Norm. Supérieure* **1923**, *40*, 325–412. [[CrossRef](#)]
79. Lifshitz, E.M.; Landau, L.D. *The Classical Theory of Fields*, 3rd ed.; Pergamon Press: Oxford, UK, 1971; Volume 2, ISBN 0750627689. First published 1923. (In Russian).
80. Eshelby, J.D. The Force on an Elastic Singularity. *Philos. Trans. R. Soc. Lond. Math. Phys. Sci.* **1951**, *244*, 87–112. [[CrossRef](#)]
81. Eshelby, J.D. The Elastic Energy-Momentum Tensor. *J. Elast.* **1975**, *5*, 321–335. [[CrossRef](#)]
82. Epstein, M.; Elzanowski, M. *Material Inhomogeneities and Their Evolutions*; Springer: Berlin/Heidelberg, Germany, 2007. [[CrossRef](#)]
83. Epstein, M.; Maugin, G.A. The energy—Momentum tensor and material uniformity in finite elasticity. *Acta Mech.* **1990**, *83*, 127–133. [[CrossRef](#)]

**Disclaimer/Publisher's Note:** The statements, opinions and data contained in all publications are solely those of the individual author(s) and contributor(s) and not of MDPI and/or the editor(s). MDPI and/or the editor(s) disclaim responsibility for any injury to people or property resulting from any ideas, methods, instructions or products referred to in the content.